energies

MDPI

Article

Surrogate Modeling and Aeroelastic Analysis of a Wind Turbine with Down-Regulation, Power Boosting, and IBC Capabilities

Vasilis Pettas * and Po Wen Cheng

Stuttgart Wind Energy (SWE), University of Stuttgart, 70569 Stuttgart, Germany; cheng@ifb.uni-stuttgart.de
* Correspondence: pettas@ifb.uni-stuttgart.de

Abstract: As the maturity and complexity of wind energy systems increase, the operation of wind turbines in wind farms needs to be adjustable in order to provide flexibility to the grid operators and optimize operations through wind farm control. An important aspect of this is monitoring and managing the structural reliability of the wind turbines in terms of fatigue loading. Additionally, in order to perform optimization, uncertainty analyses, condition monitoring, and other tasks, fast and accurate models of the turbine response are required. To address these challenges, we present the controller tuning and surrogate modeling for a wind turbine that is able to vary its power level in both down-regulation and power-boosting modes, as well as reducing loads with an individual blade control loop. Two methods to derive the setpoints for down-regulation are discussed and implemented. The response of the turbine, in terms of loads, power, and other metrics, for relevant operating conditions and for all control modes is captured by a data-driven surrogate model based on aeroelastic simulations following two regression approaches: a spline-based interpolation and a Gaussian process regression model. The uncertainty of the surrogate models is quantified, showing a good agreement with the simulation with a mean absolute error lower than 4% for all quantities considered. Based on the surrogate model, the aeroelastic response of the entire wind turbine for the different control modes and their combination is analyzed to shed light on the implications of the control strategies on the fatigue loading of the various components.

Keywords: wind turbine control; surrogate modeling; loads and control of wind turbines

check for updates

Citation: Pettas, V.; Cheng, P.W. Surrogate Modeling and Aeroelastic Analysis of a Wind Turbine with Down-Regulation, Power Boosting, and IBC Capabilities. *Energies* **2024**, *17*, 1284. https://doi.org/10.3390/en17061284

Academic Editor: Oscar Barambones

Received: 28 December 2023
Revised: 22 February 2024
Accepted: 29 February 2024
Published: 7 March 2024

Copyright: © 2024 by the authors. Licensee MDPI, Basel, Switzerland. This article is an open access article distributed under the terms and conditions of the Creative Commons Attribution (CC BY) license (https://creativecommons.org/licenses/by/4.0/).

1. Introduction

Wind energy has increased its share in the electricity generation mix and has become a pivotal technology for the global energy transition goals. The technology has matured and scaled up, leading to new research challenges beyond the optimization of the wind turbine design. The system-level optimization is becoming relevant in terms of farm-wide operation and better integration into the electrical grid. To address these challenges, wind farm control has multiple objectives that have to be considered simultaneously [1,2]. Among others, these include being able to adjust the wind farm power output accurately according to the grid demands providing flexibility, reducing the power production losses due to wake interactions, reducing the operational costs, extending the lifetime of the machines as much as possible [3–5], as well as maintaining profitability for the operators to maintain the financial attractiveness of projects [5–7]. In order to leverage the potential of digitalization and optimization towards these goals, an important aspect is to have models that can predict quickly and accurately enough the response of the entire turbine including power production and structural loads, for various operating modes and wind conditions replacing the computationally expensive aeroelastic simulations.

In this context, the contribution of the present work is to develop and evaluate a surrogate model of a wind turbine with a control system that enables the operation in various modes including down-regulation, power boosting, and individual blade control (IBC). The controller modifications required, compared to a standard baseline wind turbine

controller, are discussed including two approaches for performing the down-regulation. Two surrogate model approaches with increasing cost and complexity are developed and evaluated in terms of prediction uncertainty based on a comprehensive validation set of aeroelastic simulations. Finally, using the developed surrogate models, the aeroelastic response of the wind turbine is evaluated focusing on the trade-offs between loads and power for different conditions and modes providing insights that can be leveraged in future optimization studies. The surrogate models and datasets developed are made publicly available for further use by the wind energy community.

The baseline control system of a modern multi-MW, variable-speed pitch-regulated (VSPR) is responsible for the safe and optimal operation of a wind turbine. It is responsible for commanding the actions of the main wind turbine actuators adjusting the generator torque, blade pitch angle, and nacelle yaw orientation so that the turbine can produce power according to the design power curve while limiting the structural loads to the design load envelope. Moreover, additional setpoints can be included in the software to allow for the turbine to modify its output power level as well as additional control loops aiming to reduce structural loads. In this work, a simple baseline wind turbine controller is implemented for the DTU 10 MW reference wind turbine (rwt) [8] and is augmented with additional modes for down-regulation, power boosting, and IBC to identify the aeroelastic response in a wide range of possible operation conditions.

Congestion of the electrical grid, electrical grid load balancing, O&M decisions due to degradation of specific parts, and wind farm sector management for wakes are the most common cases where the wind turbine is required to reduce the power output from the baseline design values [1,9]. The goal is to produce less power for the same wind speed within its operational range. Additionally, wind farm flow control techniques employ down-regulation for induction-based control to reduce wake effects in a wind farm [2]. Moreover, operational management approaches have been proposed in the literature leveraging down-regulation to optimize revenue and loads by adapting the output power level [5,6]. Different naming conventions used interchangeably for the same process can be found in the literature including down-regulation, curtailment, derating, and throttling. In this work, the term down-regulation is used throughout.

To reduce the power output of a wind turbine, the power coefficient (C_p) has to be reduced. This can be performed by manipulating the operational characteristics of the machine in terms of tip speed ratio (TSR or λ) and/or blade pitch angle θ. Depending on the turbine's design and the intended application, different approaches can be used which will effectively change the operating point in the C_p-λ-θ and C_t-λ-θ spaces. The effect of choosing the setpoint to achieve down-regulation on the structural loading of the wind turbine has been investigated in ref. [9–12]. For example, for induction control applications the aim would be to minimize the thrust to reduce the wake effects; for O&M, specific reduction in the rotational speed of the rotor (ω) might be targeted, etc. No matter what the setpoint choice is, the reduction in power production comes with a reduction in structural loading as has been shown both from measurements and simulation studies [4,13,14]. In this work, we evaluate two methods for down-regulation allowing the power to be decreased up to 50% for the entire operational wind speed spectrum.

The next topic related to the controller's functionality is power boosting. This means increasing the power output of the wind turbine above the baseline rated value at higher wind speeds. Many aspects have to be considered when performing power boosting. Usually, the upper rotational speed is limited so that a maximum blade tip speed is not exceeded due to noise restrictions. Hence, this option is mostly applicable in cases of offshore wind farms where less strict limitations apply. Furthermore, the design limits of the generator and power electronics have to be considered. Electrical generators and power electronics have an upper limit of torque and power due to limitations such as electrical and thermal stresses while having some overload capacity depending on the generator design [15]. Thus, the level and time duration of possible power boost depends heavily on the design characteristics of the system. Turbine manufacturers already offer such options

in new turbines or as part of retrofit packages [16–18] aiming to optimize revenue and power production. The exact levels of power boosting are not clearly stated in all cases. From the publicly available information, an increase of 5–10% in power level by power boosting has been applied commercially. In this work, it is assumed that the electrical system of the wind turbine can handle a power boosting level of up to 30% higher than the baseline and the focus is on identifying the impact on fatigue loads. Additional methods to increase power production, e.g., aerodynamic add-ons [19], are not considered as this work focuses on software-only modifications without additional hardware modifications to a standard turbine.

One advanced control method, beyond the baseline feedback control loop, aiming for load reductions is individual pitch control (IPC). IPC leverages the fact that modern utility-scale wind turbines have an individual pitch actuator for each blade. Commanding a differential pitch angle to each blade according to some logic based on blade loads measurements can lead to structural load reductions. IPC methods have been extensively researched and field tested [20–24], and to a smaller extent applied in the industry. The reason for the scarce industrial application is on one hand the requirement of load sensors on the blade root due to cost and reliability considerations and on the other hand the longevity of the actuator and bearing due to the increased actuation which might lead to increased maintenance costs. An overview of the different concepts for individual pitch control for wind turbines along with their fundamental differences and similarities can be found in [22]. In this work, we utilize an IBC approach. IBC is based on an independent controller for each of the blades feedbacking directly the measured flapwise bending blade root bending moments and the present implementation was initially introduced in [25]. As explained in [22], the different IPC approaches are similar in load reduction effectiveness and no major differences in terms of load trends across the various turbine components are expected if an alternative approach is considered. Further advanced control methods for fatigue load reduction such as lidar-assisted control [26] or trailing edge flaps [27] are not considered as they require additional sensors and actuators to be installed on the wind turbine.

With the increase in computational power in recent years, several applications of surrogate modeling have been suggested in the context of wind energy research for uncertainty quantification, optimization, and monitoring purposes. A surrogate model, in the context of engineering modeling, is a simplified and computationally efficient representation of a complex system or process [28]. It serves as a substitute for the original model, approximating its behavior while reducing computational costs. Surrogate models are often constructed using statistical techniques or machine learning algorithms, leveraging available data to emulate the responses of the original system.

Surrogate models have been used to capture the response of a single wind turbine over a complete environmental contour, i.e., considering all wind characteristics and their possible combinations, to derive lifetime load estimations [29] and estimate lifetime reliability indices [30]. For the high dimensionality and sparse sampling considered, Kriging showed to perform better among the considered methods, depending on the computational resources availability. Polynomial response surfaces were used in [31] to analyze the sensitivity of loads for an onshore wind turbine to various input conditions. Moreover, surrogate models have been applied to perform uncertainty quantification studies considering the uncertainty propagation from aeroelastic simulations to annual energy production and lifetime loads using the polynomial chaos expansion method [32]. In [33], surrogate models are employed to quantify the propagation of uncertainty from inflow conditions and blade aerodynamic properties to loads and annual energy production where Kriging proved to perform better. Furthermore, surrogates have been used for optimization to reduce the otherwise infeasible simulation costs as shown, e.g., in [34] where they were used to optimize the design of an aeroelastically tailored blade tip extension. Surrogate models have also been proposed for capturing the load and power response of a wind turbine within a wind farm considering the farm flow effects enabling further optimization of the complex

farm system [35–37]. Polynomial chaos expansion and Gaussian Process Regression (GPR) proved to be the best-performing surrogate modeling approaches in this context.

As seen from the previous discussion, various applications of surrogate models have been successfully demonstrated in the context of wind energy research. In this work, the scope of the surrogate model is to replace the expensive aeroelastic simulations with a quick and accurate data-driven model that can be used for various purposes such as optimization or condition monitoring. The goal is to have a model that can reproduce the statistical values derived from post-processing the output time series of the simulations in terms of quantities of interest (e.g., damage equivalent loads (DELs), mean values, etc.). Therefore, the output space can be mapped thoroughly in a continuous manner to the input space, which includes the wind conditions and the controller mode. In this process, the balance between the computational cost of creating the training dataset and the prediction uncertainty has to be considered. In this work, two methods are considered and compared. A spline-based regression and the more complex and computationally expensive GPR approach.

In summary, the scope of this work is to:

- Discuss the controller design for a wind turbine able to perform down-regulation, and power boosting as well as the optional application of an IBC loop.
- Create surrogate models for the entire wind turbine system able to capture the response of the turbine according to wind conditions and control mode. Compare two approaches for this task and quantify the uncertainty.
- Analyze the aeroelastic response of the entire system of the wind turbine for different control modes across the whole operational condition envelope, focusing on trade-offs in loads and power between the various control modes that could be potentially leveraged for optimization.

The rest of the manuscript is organized as follows: In Section 2 the controller design for the different modes is discussed. Section 3 explains the process of creating a surrogate model of the turbine response with two methods. The uncertainty quantification of the surrogate's response for all quantities of interest and input conditions is performed in Section 4. The impacts of the different control modes on power, loads, and blade pitch actuation are examined in Section 5. In Section 6, the main findings are discussed qualitatively, focusing on the trade-offs between power and loads for the different controller modes and the potential for optimization. The conclusions and outlook of the work are discussed in Section 7.

2. Controller Design

2.1. Baseline Controller Design

The baseline controller described here serves as a simple control algorithm for the DTU 10 MW rwt [8]. The considered inputs of the controller are the low-pass filtered generator rotational speed and the blade pitch angle. The outputs include the commanded generator torque and the commanded collective blade pitch angle. A linear ramp is used for the transition region 1.5. In control region 2, the commanded generator torque (M_g) is based on the common $k\omega_g^2$ law tracking the optimal TSR for maximum C_p using the measured generator speed (ω_g). The collective blade pitch angle is kept constant to the θ_{fine} value in regions 1.5 and 2. The rated generator speed and rated generator torque are reached simultaneously for this turbine design, requiring no control region 2.5. In control region 3, the generator speed is controlled with a standard proportional-integral (PI) scheme with anti-windup for the pitch controller, including gain scheduling over wind speeds. The PI gains for each wind speed are tuned with the closed-loop shaping method along with manual fine-tuning considering both power and load performance. For the closed-loop shaping, a value of 0.7 was considered for the damping ratio and 0.75 rad/s for the natural frequency of the second-order linear system. This simple tuning approach ensures the stability of the closed-loop system while it also provides a consistent method to tune the gains for other power levels. Constant power is used in this region, with the applied torque

being proportional to the rotational speed. The controller's block diagram is presented in Figure 1 and the main design characteristics are provided in Table 1.

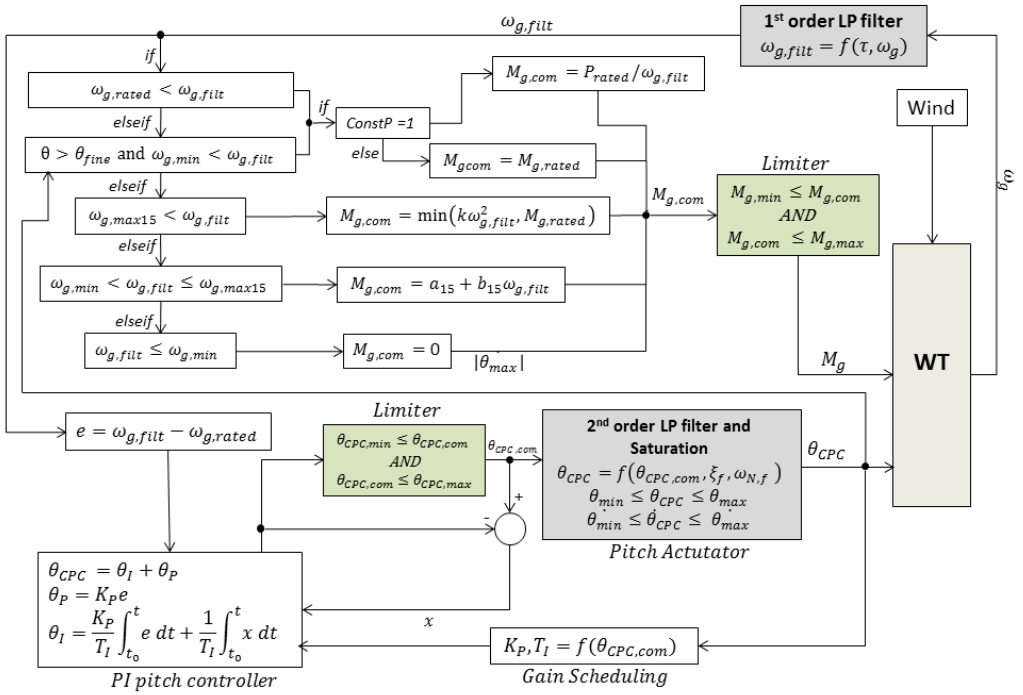

Figure 1. The two trajectories considered for the derivation of down-regulation setpoints along with the minimum C_t trajectory.

Table 1. Design characteristics of the baseline controller.

Design Characteristics	Value
Tip speed ratio	7.8
C_p	0.4669
Region 1.5 min rotational speed	5.5 rpm
Region 1.5 max rotational speed	6.0 rpm
Rated rotational speed	9.6 rpm
Rated wind speed	11.5 m/s
Torque constant for region 2	92.9748 Nm/(rad/s)^2
Cut in wind speed	4 m/s
Cut off wind speed	24 m/s
Pitch limit for switching between region 2.5–3	1 deg
Maximum generator torque overshoot allowed above rated	110 %
Generator speed first-order LP filter corner frequency	0.25 Hz

The controller and actuators are designed in Matlab/Simulink using the Sfunction version of FAST v8.16.00 [38] to perform the closed-loop aeroelastic simulations. The mechanical pitch actuator is modeled as a second-order low-pass filter with a filter frequency of 1.6 Hz and a damping ratio of 0.8. It also includes a pitch rate saturation limit of 8 deg/s. The measured generator speed is filtered using a first-order low-pass filter. There is no generator torque actuator used, assuming instantaneous response to the commanded torque. Moreover, no damping loops for drivetrain torsion and tower fore-aft vibrations are used.

2.2. Down-Regulation Mode

In this section, the trajectories followed to select the setpoints for the down-regulation, along with the changes in the baseline controller (power level = 100%, IBC not active) for achieving the desired output power level, are discussed. For this, two approaches were considered. The first keeps the TSR constant and performs the down-regulation with pitching, which will be referred to as "constTSR". The second is a linear trajectory in the C_p-λ-θ space combining both pitch and TSR modifications to achieve the reduced C_p and will be referred to as "lin70". The minimum target TSR for the lowest down regulation level of 50%, defining the second point of the linear trajectory, is 7. This limit was selected to avoid reducing further the rotational speeds. Further reduction showed to limit region 2 substantially for power levels below 65%, which has detrimental effects on power and loads as the turbine operates in off-design points for a large range of wind speeds. Additionally, further reducing the rotational speed was avoided to allow for sufficient frequency margins with the tower's first natural frequency (0.26 Hz) in region 2. The down-regulation approach of increasing the TSR was not considered to avoid increasing further the rated rotational speed and possibly introducing a control region 2.5. These choices are also aligned with the results reported in [39] where different down-regulation strategies were compared in the entire operational range accounting for cumulative DELs for a specific wind distribution. It was found that the constant TSR approach and the combination with rotor speed reduction cases are more effective in load reductions compared to the other strategies. The two selected trajectories are presented in Figure 2. The contour lines in the figure show the targeted reduction in C_p in increments of 5%.

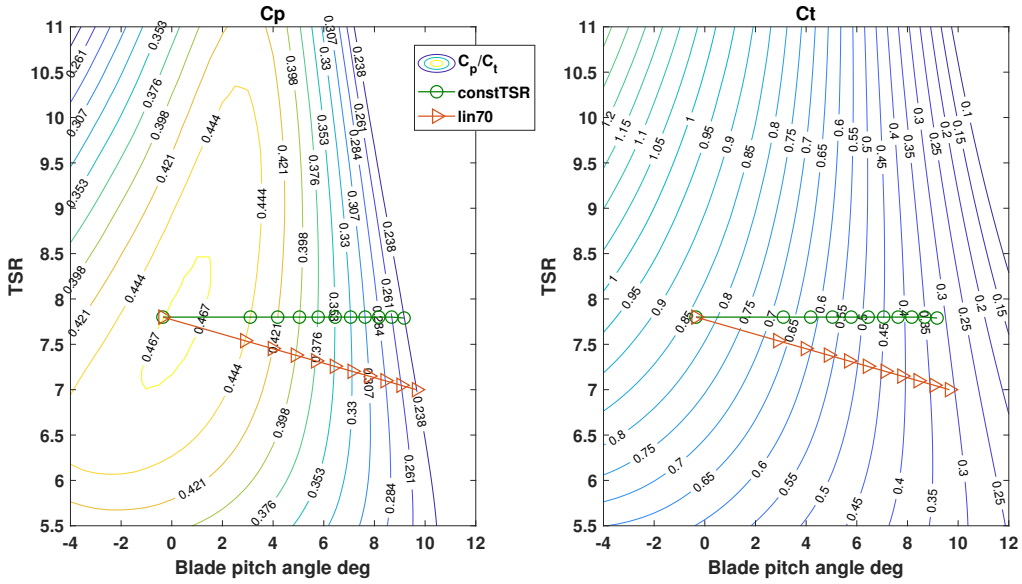

Figure 2. The two trajectories considered for the derivation of down-regulation setpoints.

Having defined the fine pitch angle and the target TSR and C_p for each level of down-regulation, the controller parameters need to be adjusted accordingly. For region 2, the adjusted torque constant k was recalculated according to the power level based on target C_p and TSR values. The adjusted value of the new rated rotational speed, required for the new setpoint definition, was identified analytically by deriving the rated wind speed based on the target C_p and TSR values.

In the full-load region, as constant power is used for every mode of the controller, the torque is again derived by the targeted rated power and instantaneous filtered generator speed. For the PI pitch controller, the new $\omega_{g,rated}$ setpoint was used, and the gains, along with the gain scheduling for different mean pitch angles, were tuned with the same process as the baseline. This allowed for a consistent dynamic behavior of the controller for all power levels while the rotor speed regulation performance was not affected.

For region 1.5, the rotational speed points defining the torque-speed ramp were kept the same as the improvements, in terms of loads and power, found by fine-tuning were minor and no consistent pattern could be identified to generalize for every power level. This approach slightly changes the effective cut-in wind speed for different power levels depending on the aerodynamic torque achieved. In practice, this means that down-regulation can be applied down to a minimum level depending on the wind speed. Moreover, exact power tracking cannot be followed in region 1.5 since the combination of the fine pitch angle and the off-design TSR can vary the C_p.

All the aforementioned parameters were derived for power levels from 50% to 100% with a step of 5% and provided as a look-up table. The values in between are calculated by linear interpolation according to the requested power level. The resulting steady-state response derived from aeroelastic simulations of the turbine for the different power levels is shown in Figure 3.

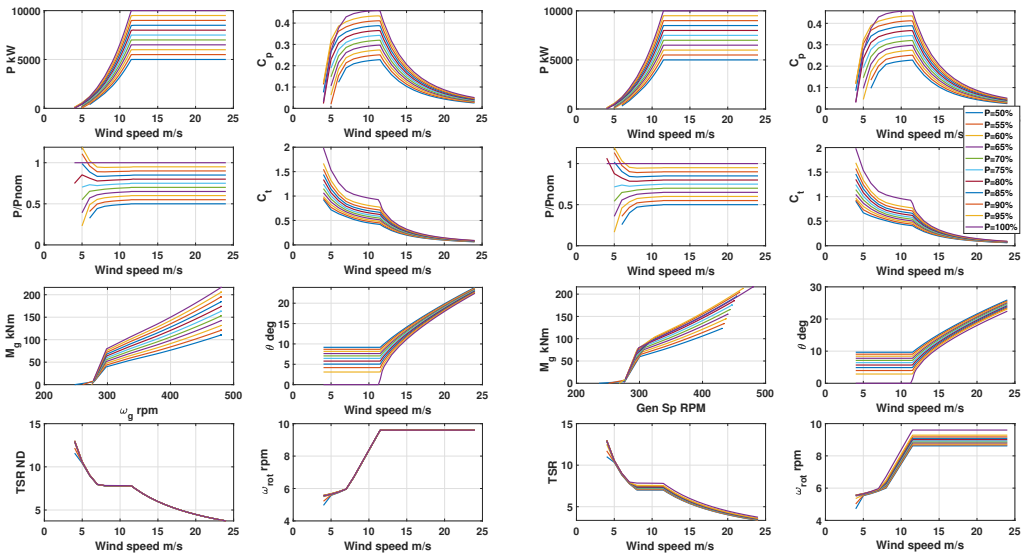

Figure 3. Steady-state operational characteristics for the two down-regulation trajectories: Left columns 1 and 2: constTSR trajectory. Right columns 3 and 4: lin70 trajectory.

Power reference tracking with both trajectories is accurate for wind speeds higher than 6 m/s. In lower wind speeds and for both trajectories, down-regulation levels higher than 75% produce power higher than targeted, even increasing above the baseline level. This can be explained by the TSR being closer to the design value, leading to increased C_p in this region. For down-regulation levels below 75%, the opposite behavior is observed. In power levels below 60% the produced aerodynamic power is not enough for electricity production, slightly shifting the cut-in wind speed.

2.3. Power Boosting Mode

The design goal of a power boosting mode is to increase the power output of the turbine in the widest possible range of wind speeds with the least possible increase in loads. Additionally, the technical limits of power boosting stemming from the generator and power electronics as well as aerodynamic considerations related to the maximum tip speed have to be considered.

The control strategy for power-boosting depends on the specific aerodynamic design characteristics of the turbine. Figure 4 presents the possible controller trajectories in the generator speed–generator torque plane based on the presented baseline controller for the DTU 10 MW rwt. Trajectory A-B represents the torque-based approach where the rated rotational speed remains the same and the torque is increased. This approach would create a vertical region 2.5 where the turbine will operate with sub-optimal C_p. The increased torque demand would be directly proportional to the power increase. Trajectory A-C follows the

optimal C_p, extending region 2 until the new power level is reached. Power boosting based on increasing only the rotational wind speed is described by trajectory A-D where after rated torque is reached, the rotor would keep speeding up as wind speed increases until the desired power level is achieved. This leads to an extended region 2.5, and the required increase in speed is directly proportional to the requested power increase. Trajectories A-E-F1 and A-E-F2 are examples of an approach increasing both speed and torque and can be adjusted to any proportion between them.

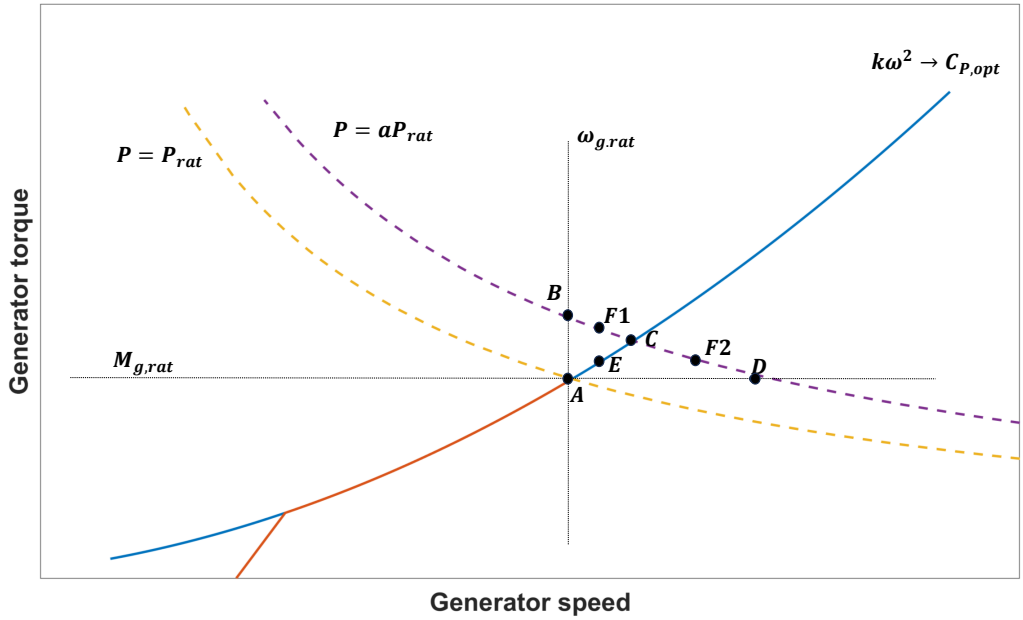

Figure 4. Power boosting controller trajectories for generator torque and speed.

The decision was to extend region 2, continuing to track optimal C_p until the new rated value is reached following the $k\omega_g^2$ method for the torque. This implementation avoids creating transition regions that would vary in range depending on the power boosting level and ensures a similar controller behavior for all power levels. Moreover, this approach was selected to avoid the maximum increase in rated torque and rotational speed values, which can potentially draw the limits of the maximum feasible power level in a real system.

The relevant changes in the controller parameters include assigning a new rated speed and rated torque and adapting the gains of the PI pitch controller. The rated values are derived analytically and used as the new setpoint for the pitch controller. The PI gains and the gain scheduling were derived for each power boosting level with the same procedure as for the baseline since the targeted C_p in higher wind speeds is higher than the baseline. With this approach, the resulting dynamic response of the controller is similar for all power levels while the performance of the controller in terms of regulating rotor speed is also consistent. All the quantities required for the power boosting were calculated for power levels between 100 and 130% with increments of 5% and provided as a look-up table. The rest of the values are derived by linear interpolation based on the requested power level.

The resulting steady-state operational characteristics for the power boosting mode are shown in Figure 5. For the maximum power level considered (130%), the increase in rotational speed and tip speed is 8.3% compared to the baseline design, with the rotor reaching a maximum rotational speed of 10.5 rpm and the blade tip a maximum translational speed of 97.6 m/s. The maximum torque is increased by 18.8%, reaching 257 kNm. The rated wind speed is increased up to 12.6 m/s.

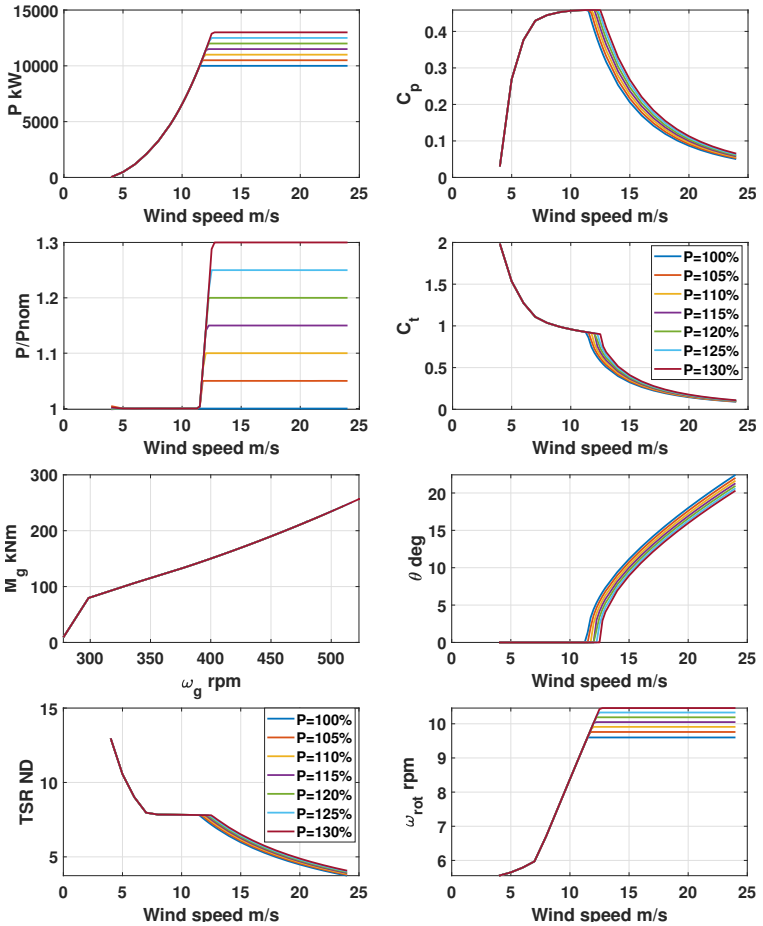

Figure 5. Steady-state operational characteristics for the power boosting mode.

2.4. Individual Blade Pitch Control

In the scope of this work, an IPC loop is added to the controller as a structural load alleviation method. The goal of the controller design is to have a simple and robust IPC loop completely decoupled from the main pitch control loop, which is responsible for the speed regulation in the full load region. The only requirement for its implementation compared to the baseline operation, except for the software change, is the addition of load sensors to the blade roots. For this, an individual blade control (IBC) approach was chosen. IBC is based on three independent controllers feedbacking directly the measured flapwise bending moments at the root of each blade. The method is based on [40,41] and was initially presented and evaluated in [25].

The IBC controller is used as an add-on to the existing baseline PI collective pitch controller (CPC) controller which is not re-tuned or otherwise changed. Therefore, the differential $\Delta\theta_{IBC}$ contribution in pitch demand of each single-input-single-output SISO controller is summed with the commanded pitch of the baseline CPC controller. IBC is active only in above-rated conditions and the switching between regions is performed based on the power signal where the IBC outputs are scaled with a factor varying linearly between 0 and 1 for power levels between 90% and 100% of the rated power. This strategy ensures smooth transitioning while minimizing power losses and enhancing load alleviation. The parameters of the scaling were assessed by manual testing in terms of power and loads through simulations around rated wind speed.

Moreover, the gains of the controller, similar to the traditional CPC controllers, are scheduled based on the collective pitch values to compensate for the non-linear dynamics and different sensitivity of pitching at different wind speeds. This was performed for three wind speeds 16, 20 and 24 m/s (and the corresponding mean pitch angle) and

linearly interpolated for the rest of the operational points. The control scheme itself is a traditional linear feedback PI structure due to its simplicity and robustness. Another important part of the IBC loop design is the combination of the filters applied on the input blade root bending moment and on the output pitch command regulating the effective bandwidth of the controller. Hence, the parameters defining the controller's behavior are the frequencies of the high pass (HP) and band stop (BS) filters, as well as the tuning of the gains. The schematic diagram of the control system is presented in Figure 6. For the present application, the actuation bandwidth of the IBC loop is restricted to the 1P as previous studies [25] showed a large trade-off between the increase in pitch actuator usage and further load reductions. More detailed information on the IBC implementation can be found in [25].

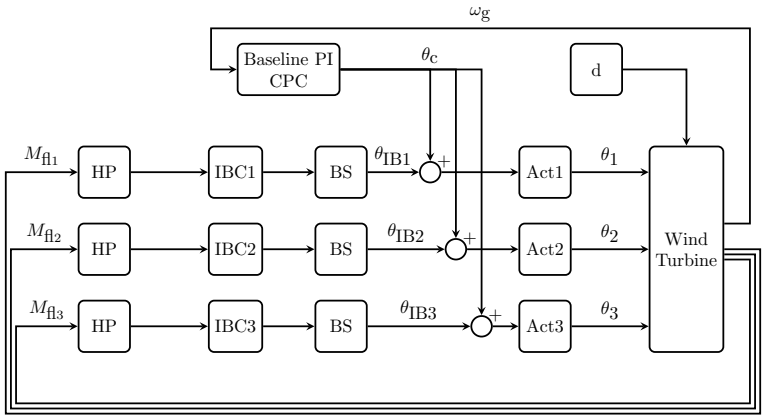

Figure 6. Block diagram of the IBC controller.

To adapt the IBC loop to the different power levels, some parameter changes are required. The HP filter was kept the same for every power level, while the frequency of the in-series BS filters was adapted according to the adjusted rated rotational speed. As the manual fine-tuning of the gain is a time-intensive procedure, it was decided to simplify the process by only tuning the gains for the other power levels in one wind speed and performing a linear regression to derive a linear function of the gain over power levels. The gain scheduling over wind speeds per power level was simply performed by offsetting the schedule derived for 100% power level and adjusting according to the mean speed corresponding to the mean CPC blade angle. This process was conducted for power levels in the range of 50–130% with a step of 5% and formulated as a look-up table. This approach can lead to slightly lower performance by the IBC loop but it is not expected to significantly influence the overall trends in load reductions and actuator usage while it simplifies the implementation. The gains and corresponding scheduling were calculated with linear interpolation for any power level between the tabulated values.

3. Surrogate Modelling

The overview of the surrogate modeling process used in this work is shown in Figure 7. The yellow blocks denote the creation of the training set based on some design of experiment (DOE) approach. The range of the input variable space has to be defined first according to the scope of application. Then, the appropriate sampling method and size for the training set have to be determined based on the computational cost constraints. Having the training set, a regression method has to be applied, allowing requests for any arbitrary value within the range of the input space to obtain the output prediction. This is the core of the surrogate model, shown in the dashed lines in the figure. Additionally, the regression model can be compared to a validation set to obtain uncertainty estimates, as shown by the blue blocks in the figure.

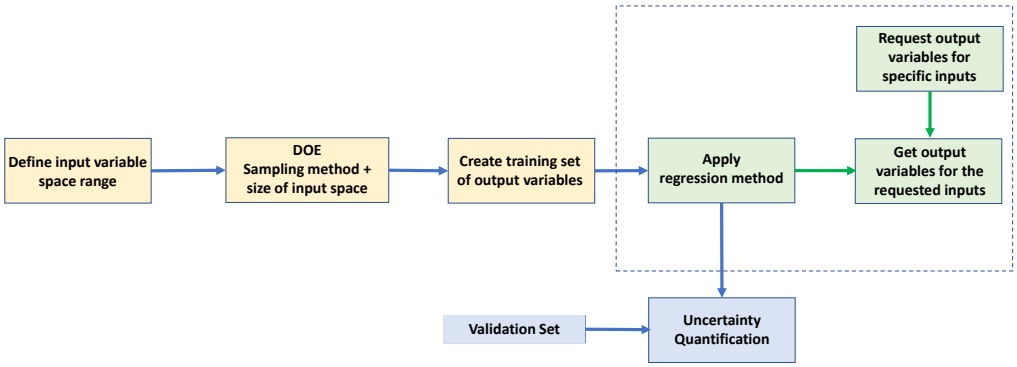

Figure 7. Overview of the procedure to create, apply and validate a surrogate model. The dashed rectangle indicates the actual surrogate model. The yellow blocks show the steps to create the training set, and the blue blocks show the uncertainty quantification.

The first step in creating the training set is to define the input variables and their range, which is application-specific and constrained by the available computational power. In most of the applications discussed in the literature, the goal is to obtain the response of the turbine for a full environmental contour (including, e.g., wind speed, TI, shear, veer, air density, etc.). This approach leads to a high dimensional input space, with more than n = 7 input variables in most cases, which makes a dense factorial sampling infeasible due to the computational cost as the sample size scales with the power of n.

In the present application, the goal is to capture the response of a single onshore turbine operating with different control modes. Hence, no wind farm flow effects are considered. Furthermore, it is assumed that the turbine operates with no yaw misalignment (intentional or not). According to the IEC standard 61400-1 for wind turbine design [42], the main inflow conditions that need to be considered for load assessment are the mean hub height wind speed, turbulence intensity (TI), wind shear, air density, and vertical flow angle. The vertical flow angle is site-specific, which means it can be accounted for as a fixed independent input variable. In this work, it is considered to be 0 degrees. As previous studies have shown (see, e.g., [31,43,44]), the most influential characteristics for fatigue loads are the mean wind speed and the turbulence intensity, with the wind shear following. To reduce dimensionality but also due to the fact that wind shear measurements are commonly not available in the operational stage, it was decided to keep it constant to the conservative value of 0.2 as suggested by the IEC standard.

With these considerations, the input variable space is three-dimensional, including mean wind speed, TI, and controller mode. Additionally, to account for the seed-to-seed variability, three stochastic wind field realizations are used for each combination of wind conditions. The duration of the simulations is set to 3600 s while including an additional 100 s interval at the beginning of each simulation to remove transient numerical effects. The longer time duration, compared to the commonly used 600 s, reduces the seed-to-seed variability and includes more low-frequency components that can potentially influence loads.

The limited input variable space allows for a full factorial sampling DOE approach. For the available computational setup, the aeroelastic simulation time is approximately three times the real-time, making a dense sampling feasible. The wind speeds are discretized with a step of 1 m/s from cut-in to cut-out. TI ranges from 2 to 24% with a 2% step. The power level is discretized from 50 to 130% with a step of 5% with both down-regulation strategies (constTSR and lin70) considered. Power boosting and IBC modes are simulated for wind speeds >10 m/s. The resulting amount of unique wind fields generated is 756, and the total number of simulations performed is 24,912. An overview of the variable space and simulation parameters is given in Table 2.

Table 2. Variables and parameters for the simulations used to create the training set.

Variable/Parameter	Values
Wind speed	4:1:24 m/s
TI	2:2:24%
Shear PL exponent	0.2
Air density	1.225 kg/m^3
Inflow angle	0 deg
Yaw misalignment	0 deg
Power level	50:5:130%
IBC	On/Off (for wsp > 10 m/s)
Turbulence seeds	3
Turbulence model	IEC Kaimal
Surface roughness	0.03 m
Simulation duration	3600 s
Simulation time step	0.025 s

The aeroelastic simulations were performed with the mid-fidelity, open-source tool FAST v8.16.00 [38,45] provided by the National Renewable Energy Laboratory (NREL). All degrees of freedom available in the structural module ElastoDyn were enabled besides the *YawDOF* option, as the nacelle yaw is maintained constant throughout the simulations. In the aerodynamics module AeroDyn v14.04, the Beddoes dynamic stall model was activated. Additionally, the equilibrium induction-factor model, along with the Prandtl corrections for tip-loss and hub-loss calculations, were used. Moreover, the tower shadow model was deactivated. The settings regarding the turbine configuration and the various modules used in FAST were kept consistent for all simulations. The FAST software was compiled as an S-function and integrated within a Matlab/Simulink framework. The controller and actuators were designed in Matlab and connected to the S-function within the aforementioned simulation framework. More information on the turbine model and its implementation in FAST can be found in [8,46].

The open-source software Turbsim v2.0.0 [47], provided by NREL, was used for generating the numerical wind fields. The grid dimensions were set to 180 by 180 m with 31 grid points along each dimension. The time step of the wind fields was set to 0.125 s. The turbulence model used was the International Electrotechnical Commission (IEC) Kaimal model by enabling the *IECKAI* option along with the IEC normal turbulence model and the default surface roughness length options in Turbsim. The power law model was used for the wind shear. All settings were kept constant for all wind fields generated.

The time series outputs for the quantities of interest are post-processed to derive the target metrics. The three seeds are used to derive the mean value and standard deviation for each operational point. The processed metrics are then tabulated in 3D matrices having dimensions: wind speed, TI, and power level. In total, four independent matrices, per metric considered, are created for the different control modes and their combinations: constTSR, constTSR_IPC, lin70, and lin70_IPC. These four matrices are the training datasets on which the regression methods are applied.

The DELs are calculated based on Miner's rule [48] for linear damage accumulation using the rainflow-counting algorithm [49]. The DELs are calculated using Equation (1) where j is the total amount of binned load ranges, S_i is the mean value of the i_{th} load range bin, N_i is the number of cycles counted for this load range, N_{eq} is the equivalent number of cycles, and m denotes the Wöhler exponent. A value of $m = 4$ is used for all steel components, while for the blades, a Wöhler exponent of 10 is considered. The 1 Hz DEL is calculated for all cases using an N_{eq} of 3600 since the simulations have an hourly duration.

$$DEL = \left(\sum_{i=1}^{i=j} \frac{N_i}{N_{eq}} S_i^m \right)^{1/m} \quad (1)$$

In addition to DELs, the metrics considered include the mean, standard deviation, minimum and maximum values for each quantity. Furthermore, the energy production is calculated by integrating the electrical power signal over the duration of the simulation and the blade pitch travel is calculated using Equation (2) to obtain a metric of the impact of the different control modes on the blade pitch actuator.

$$PitchTr = \sum_{t=t_o}^{t=t_{end}-1} |\theta_{t+1} - \theta_t| \quad (2)$$

Additionally to the training dataset, a validation dataset was created. The scope of the validation set is to assess the performance of the surrogate model in terms of predictive accuracy by comparing the surrogate response to unseen data. For the validation set, only one control mode was considered, using the constTSR trajectory for down-regulation without IBC. This was performed to reduce the required sampling size to effectively cover the input space, as the general trends are similar for the different controller modes. The validation set consists of 200 unique points derived using the Latin hypercube method [50] and is shown in Figure 8. The entire variable space was sampled for the wind speed and power level input variables, while for TI, the interval considered was 2–18%.

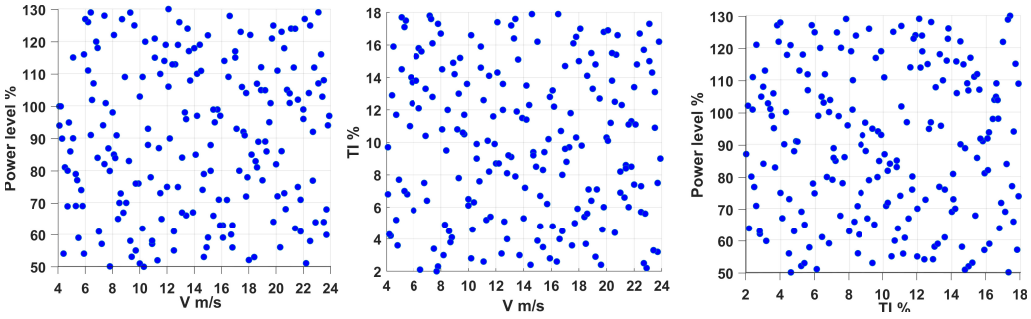

Figure 8. Sampling of validation set based on the latin hypercube method.

After obtaining the training and validation datasets, the next step is to perform the regression. Before applying the regression methods, an additional step of smoothing the training dataset is performed. The filtering for each of the four matrices was performed using a 3D Gaussian filter with a convolution kernel size of $3 \times 3 \times 3$ points and a standard deviation of 0.6. These values were derived iteratively, aiming for a filter that smoothes local peaks but does not change the general trends or increase the uncertainty metrics considered.

Two regression methods are considered: a spline-based interpolation and a GPR model. The spline-based interpolation is a straightforward and efficient regression technique selected for its simplicity, ease of implementation, and fast prediction capabilities. It serves as a baseline method to compare against the more computationally demanding GPR model, identified in the literature as one of the best-performing methods for the application. The objective is to assess whether the increased computational cost associated with GPR yields any advantages for the specific task under consideration.

Spline-based interpolation involves fitting a smooth curve or surface, called a spline, through the given data points. The spline is composed of piecewise-defined polynomial functions that ensure continuity and smoothness across the entire interpolation region. This technique is used to generate continuous and differentiable approximations of the underlying data, enabling accurate representations. It is often preferred to pure polynomial interpolation using a single polynomial to fit the whole dataset. Spline interpolation produces similar results, even when using lower-degree piecewise polynomials, while avoiding the issues with using single higher-degree polynomials that can lead to rippling near the edges of the interpolation interval. In this work, cubic splines are used with not-a-knot end conditions. Thus, at the first and last interior break, even the third derivative is continuous.

GPR (also referred to as Kriging) is a statistical modeling technique used to estimate and predict values in a continuous domain. It is based on the concept of Gaussian processes, which are collections of random variables that jointly follow a multivariate Gaussian distribution. In GPR, a Gaussian process is used to model the underlying relationship between input variables and corresponding output values [28,51]. By leveraging the assumption of smoothness and incorporating prior knowledge, GPR provides a flexible framework for interpolation and extrapolation. It estimates not only the mean prediction but also provides uncertainty estimates associated with each prediction.

GPR aims to model the relationship between input variables (X) and output variables (y) using a Gaussian process. A Gaussian process is characterized by its mean function $\mu(x)$ and a covariance function $k(x, x')$. The mean function represents the expected value of the output variable at any given input point, while the covariance function quantifies the similarity between output variables at different input points.

It is assumed that the output variable follows a Gaussian distribution: $y = f(x) + \epsilon$, where ϵ is Gaussian noise with mean zero and variance σ^2. The goal is to predict the output variable y^* for a new input x^* given a training dataset with input-output pairs (X, y). The predictive distribution of y^* given the training data is also Gaussian: $p(y^*|x^*, X, y)\ N(\mu^*, \sigma^2)$. The mean μ^* and variance σ^{*2} of the predictive distribution can be computed using the training data and covariance function. Specifically, the mean and variance are given by:

$$\mu^* = k(x^*, X)(K + \sigma^2 I)^{-1} y \tag{3}$$

$$\sigma^{*2} = k(x, x^*) - k(x^*, X)(K + \sigma^2 I)^{-1} k(X, x^*) \tag{4}$$

where k is the covariance function (kernel function), $K = k(X, X')$ is the covariance kernel matrix where its entries correspond to the covariance function evaluated at the observations.

The choice of covariance function, such as the squared exponential, Matérn, or rational quadratic, along with its hyperparameters, determines the smoothness and complexity of the resulting regression model. These hyperparameters can be optimized based on the data using maximum likelihood estimation or other methods. Model selection and evaluation in Gaussian process regression can be performed using techniques like cross-validation or Bayesian model comparison. More details on the mathematical implementation of GPR can be found in [51].

In this work, GPR is implemented using the native Matlab implementation framework provided by the machine learning toolbox. For each quantity of interest, a separate GPR model is trained using the response data from the training set for the three input variables. This approach allows for fine-tuning the parameters individually for each response and ensures accuracy by accommodating different scales and smoothness characteristics of the response signals. For each quantity of interest, hyperparameter optimization was performed using the Matlab framework provided with the *fitrgp* library using the random search optimization method. The chosen kernel and radial basis functions for the GPR models are presented in Table A1. The noise standard deviation input was set close to zero since, in this work, the regression results are treated in a deterministic manner. However, for probabilistic assessment, the noise can be adjusted point-wise based on the standard deviation of the three seeds. The training set, along with the trained GPR models and relevant reading functions, are publicly available at https://doi.org/10.5281/zenodo.10092271 (accessed on 15 December 2023).

4. Uncertainty Quantification of the Surrogate Response

The surrogate models are evaluated by comparing them to the validation set to assess the performance of the two regression methods. Additionally, the uncertainty associated with each quantity of interest is quantified. The objective is to determine the overall level of uncertainty for each quantity and identify the specific conditions where the highest uncertainty is observed.

The box plots of the relative error and relative absolute error in percentage are shown in Figure 9 for both methods. An overview of all the mean errors (ME), mean absolute errors (MAE), median absolute errors (MedAE), and coefficients of determination (R^2) for all quantities of interest for both regression methods are shown in Table 3.

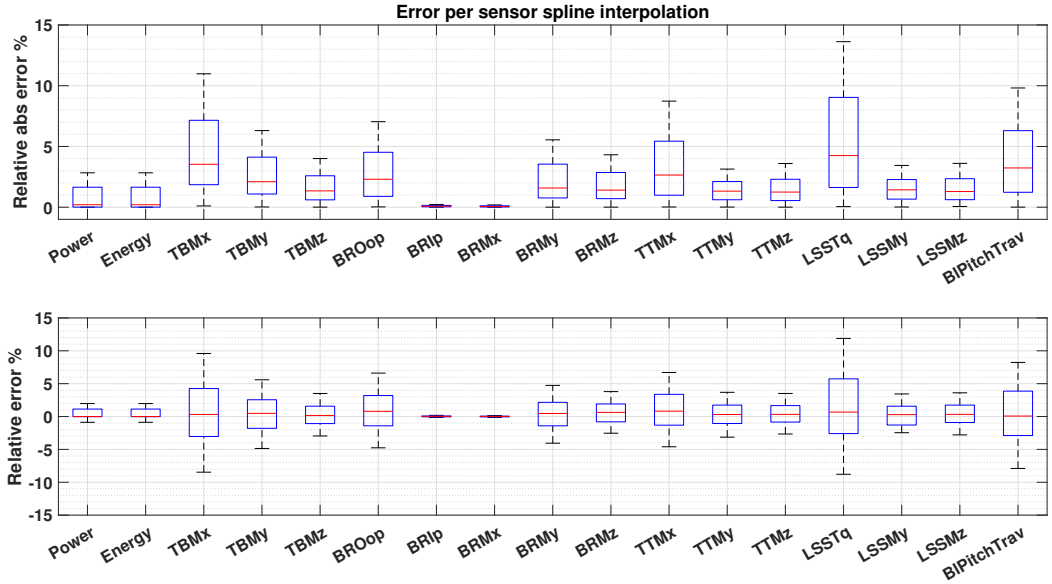

(**a**)

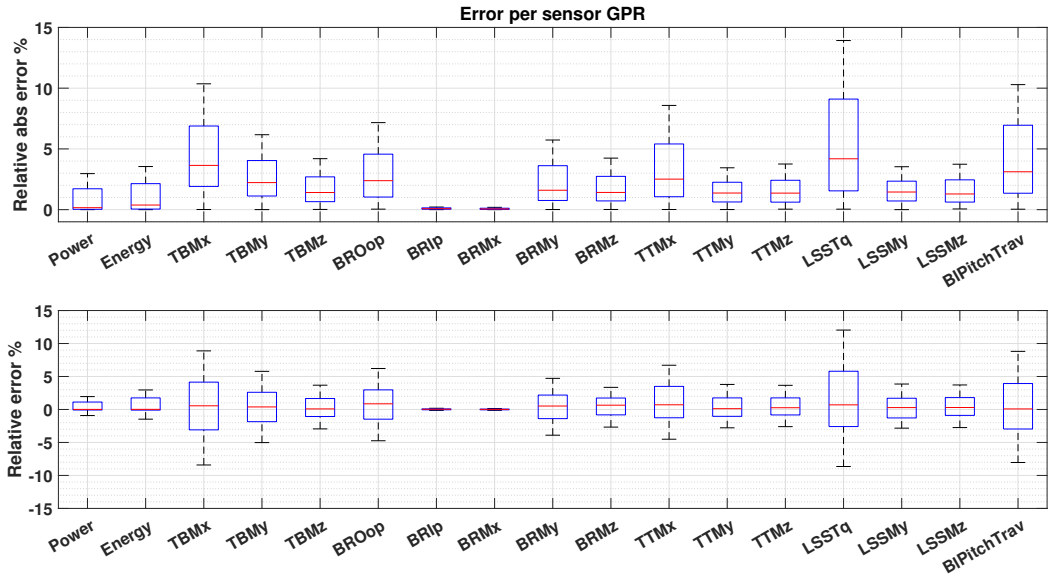

(**b**)

Figure 9. Box plots of the relative error and relative absolute error for the spline interpolation (**a**) and the GPR model (**b**) to the validation set per sensor. The central mark indicates the median, and the bottom and top edges of the box indicate the 25th and 75th percentiles, respectively. The whiskers extend to the maximum and minimum values not considered outliers. Outliers are defined as values greater or smaller than the quartile value plus/minus 1.5 times the interquartile range.

Table 3. Evaluation metrics of the GPR and spline-based surrogate models compared to the validation set. ME: mean error%, MAE: mean absolute error%, MedAE: median absolute error%, R^2: coefficient of determination. s denotes the spline-based interpolation and g the GPR model

Quantity	ME s	ME g	MAE s	MAE g	MedAE s	MedAE g	R^2 s	R^2 g
BRMx	0.0	0.0	0.1	0.1	0.1	0.1	0.9981	09981
BRMy	0.6	0.6	2.4	2.5	1.6	1.6	0.9966	0.9966
BRMz	0.6	0.6	2.1	2.1	1.4	1.4	0.9936	0.9937
BROop	0.8	0.8	3.0	3.0	2.3	2.4	0.9950	0.9951
BRIp	0.0	0.0	0.1	0.1	0.1	0.1	0.9987	0.9987
TBMx	0.6	0.6	4.9	4.9	3.5	3.6	0.9915	0.9916
TBMy	0.5	0.6	3.2	3.2	2.1	2.2	0.9914	0.9913
TBMz	−0.6	−0.5	2.6	2.7	1.3	1.4	0.9987	0.9987
TTMx	1.3	1.3	4.0	4.1	2.6	2.5	0.9933	0.9934
TTMy	0.7	0.7	1.8	1.9	1.3	1.4	0.9990	0.9990
TTMz	0.6	0.6	1.7	1.8	1.2	1.3	0.9990	0.9990
LSSMy	0.6	0.7	1.8	1.9	1.4	1.5	0.9990	0.9990
LSSMz	0.6	0.8	1.8	2.0	1.3	1.3	0.9990	0.9990
LSSTq	1.8	1.9	6.7	6.8	4.2	4.2	0.9584	0.9580
Power	1.8	2.0	3.3	3.6	0.2	0.1	0.9998	0.9998
Energy	2.0	1.9	2.8	4.4	0.2	0.4	0.9998	0.9997
PitchTr	1.9	2.1	11.6	11.2	3.2	3.1	0.9927	0.9928

Comparing the two methods and their uncertainty metrics, it is shown that they have practically the same level of accuracy with small discrepancies in the level of decimals in percentage. This indicates that, for the present application and the dense factorial sampling considered, there is no significant benefit in accuracy by using the GPR model. The main benefit of employing the GPR model would be its ability to provide uncertainty estimates for each prediction that can be used for uncertainty propagation studies. The disadvantages of the GPR model compared to the spline-based interpolation are the computational time for training, the size of the model, and the longer time to produce the predictions. The higher computational cost can be a disadvantage if the model is used in the context of optimization where multiple calls might be required.

To understand the uncertainties of the surrogate model better, the different quantities of interest are analyzed individually. As both surrogate approaches behave similarly, only the GPR model will be used for this analysis. In Figure 10, the comparison of the surrogate response to the validation set is shown for all quantities.

The blade root edgewise and in-plane loads, BRMx and BRIp, are captured with very high accuracy with a MAE of less than 0.2%. This is expected as these loads are mainly driven by rotational speed and gravity. The blade root flapwise and torsional loads, BRMy and BRMz, have an MAE smaller than 2.5%. Figure 11 shows the error sorted per input variable for these loads. The uncertainty in both cases is influenced the most by TI as the error scatter increases with increasing TI. Moreover, BRMz uncertainty is higher for above-rated wind speeds, which can be attributed to pitch control activation as torsional blade loads are increased with pitching, and the exact pitching behavior depends on the stochastic behavior of the wind. At low wind speeds < 5 m/s, higher error values can be seen in both cases. Here, the controller is in region 1.5, and depending on the turbulence, the wind speed can go below cut-in or operate in region 2 for different periods, making the results sensitive to these changes. Additionally, the absolute values are very small in this region, which has a magnifying effect on the errors. Small changes in the absolute value lead to high changes in the relative error. This observation can be generalized for most of the output quantities considered.

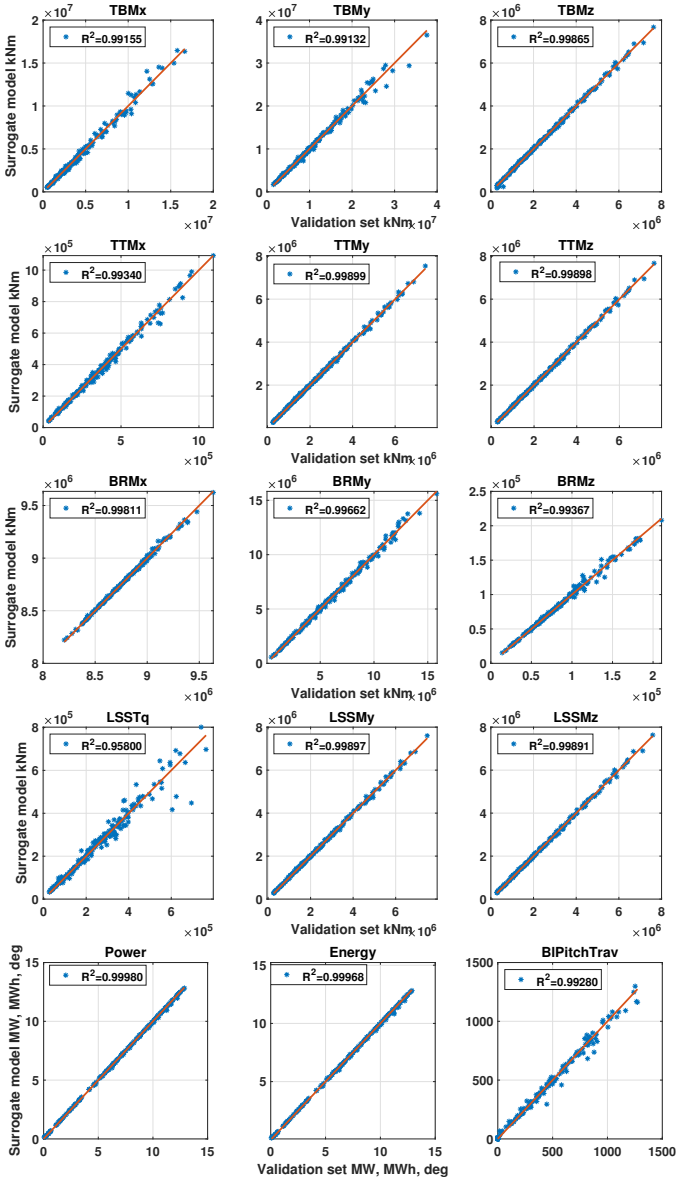

Figure 10. Comparison per sensor between the surrogate response and the validation set using the GPR regression and the constTSR trajectory for down-regulation. Legends include the coefficient of determination R^2. The identity line is plotted in red.

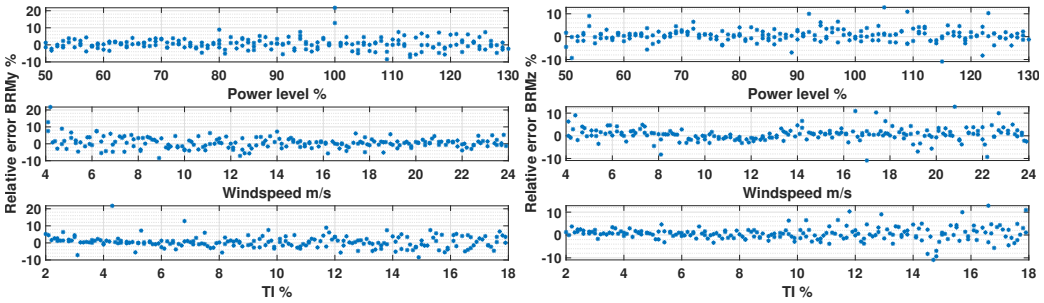

Figure 11. Relative error between the surrogate predictions and the validation dataset sorted per input variable. (**Left**): blade root flapwise moment DEL. (**Right**): blade root torsion DEL.

The tower bottom load with the least uncertainty is the torsional load TBMz. The MAE is 2.7% with the highest errors in the very low wind speeds <5 m/s. The MAE for the tower bottom side-side and fore-aft loads, TBMx and TBMy, is 4.9% and 3.2%, respectively.

The relative error sorted by the input variables for these loads is shown in Figure 12. TBMx has the second-highest error values from all the loads considered. As the side-side component is less damped by the aerodynamic forces, it presents a more stochastic loading behavior over wind speeds. It has a higher dependency on the turbulence seed realization, which leads to higher uncertainty for the surrogate model. For the TBMy load, higher uncertainty is observed for low TI (<4%), with the surrogate consistently overestimating the output. Moreover, a weaker correlation between increased uncertainty with increased load magnitudes (seen in Figure 10) is observed. The highest fore-aft loads are observed around the rated wind speed, due to the controller transition between the partial and full load as well as the high aerodynamic thrust, which is a region of higher uncertainty for TBMy.

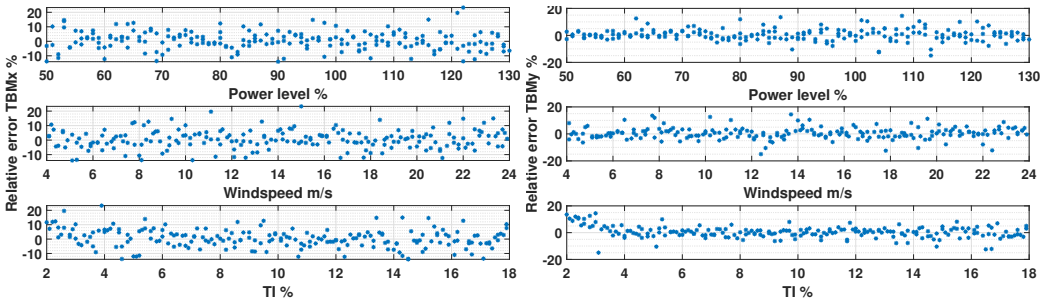

Figure 12. Relative error between the surrogate predictions and the validation dataset sorted per input variable. (**Left**): tower bottom side-side moment DEL. (**Right**): tower bottom fore-aft moment DEL.

The tower top pitch and yaw moment loads, TTMy and TTMz, exhibit very similar patterns in terms of error magnitudes and uncertainty distribution. The relative error sorted by the input variables for the tower top roll and yaw moment, TTMx and TTMz, is shown in Figure 13. For these loads, the MAE is 4.1% and 1.9%, respectively. In the case of TTMx, the uncertainty is primarily driven by wind speeds, with the highest values observed in below-rated wind speeds and the uncertainty increasing as wind speeds decrease. As the roll moments are correlated with the variation in rotor speed and generator torque, the DELs in below-rated regions, and especially in region 1.5, have the highest variation leading to high sensitivity of loads to conditions. This translates to higher prediction uncertainty for the surrogate model. For TTMy and TTMz there is no clear trend of correlation of uncertainty to input variables. In most cases, increased uncertainty is observed for very low wind speeds (<5 m/s).

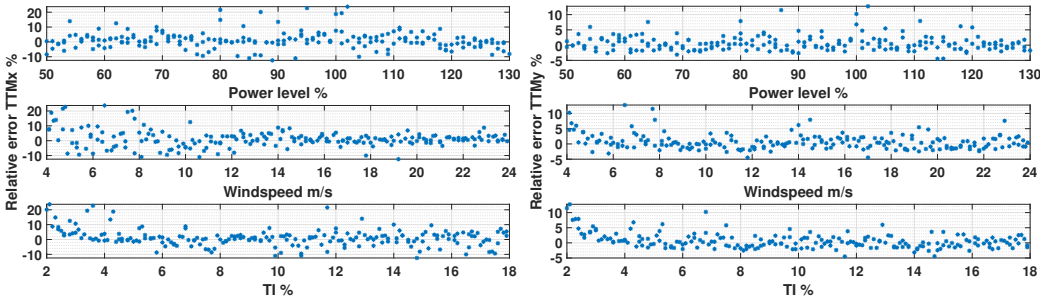

Figure 13. Relative error between the surrogate predictions and the validation dataset sorted per input variable. (**Left**): tower top roll moment TTMx DEL. (**Right**): tower top pitch moment TTMy DEL.

Low-speed shaft bending moment loads, LSSMy and LSSMz, present very similar patterns in terms of error magnitudes and uncertainty distribution. The relative error sorted by the input variables for LSSMy and low-speed shaft torque, LSSTq, is shown in Figure 14. For LSSMy and LSSMz, the MAE is 2%. There is no clear pattern of dependency of uncertainty to input variables. The LSSTq load has the highest uncertainty from all loads considered, with an MAE of 6.8% and the lowest coefficient of determination. As seen from the direct comparison in Figure 10, the highest uncertainty is correlated with the

highest magnitudes, which in turn occur in the transition region around rated. This is also confirmed in Figure 13, where higher errors are observed in this region.

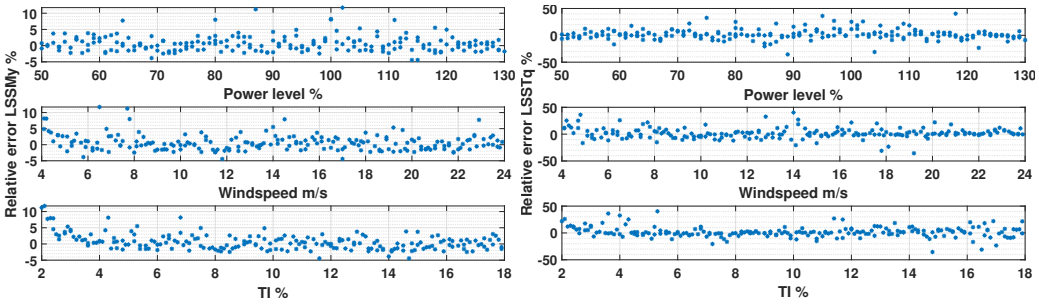

Figure 14. Relative error between the surrogate predictions and the validation dataset sorted per input variable. (**Left**): low-speed shaft moment around y-axis LSSMy DEL. (**Right**): low-speed shaft torque LSSTq DEL.

Power, energy, and blade pitch are also captured by the surrogate. The relative error sorted by the input variables for these is shown in Figure 15. Power and energy are highly correlated in terms of error magnitudes and uncertainty distribution. The reported MAE values close to 4% can be misleading as the high error values are primarily observed at very low wind speeds below 5 m/s. In this region, even small changes in wind speed can lead to larger errors, although the absolute difference in power is only a few kW. If only speeds above 5 m/s are considered for the calculation of MAE, the value becomes 0.4% and the highest uncertainty is observed in the transition region around rated wind speed. The blade pitch travel output has an MAE of 11.2%. As seen in the figure, larger errors are observed in the rated and slightly below-rated wind speeds. Since the transition to region 3 depends on the variation of wind speeds, the pitch travel magnitude depends highly on the specific turbulent realization leading to higher uncertainty for the surrogate model in this region. This is confirmed if only samples with wind speed >12 m/s are considered; then the MAE becomes 4% (not shown in the figure).

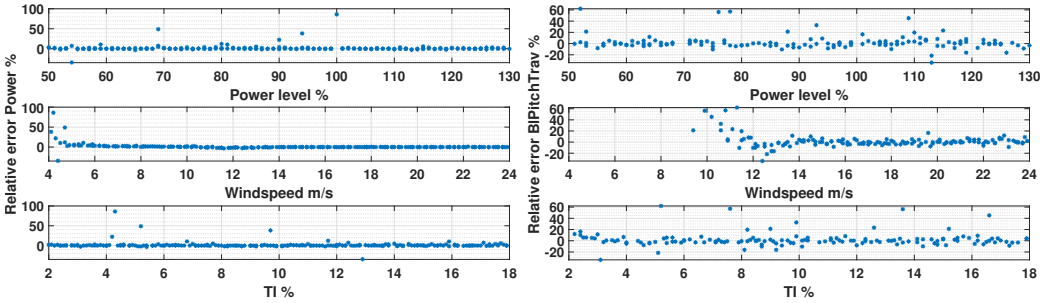

Figure 15. Relative error between the surrogate predictions and the validation dataset sorted per input variable. (**Left**): mean electrical power. (**Right**): blade pitch travel.

5. Aero-Servo-Elastic Analysis

The response of the wind turbine is analyzed using the surrogate response for the different control models and input conditions. Only the GPR surrogate is used, as the response between the two surrogate methods was found to be similar. The goal is to identify the trends of loads for the entire system, power, and pitch travel for the considered range of input variables, as well as the effect of the IBC loop and the two down-regulation trajectories. This analysis provides a better insight into the dependency of the loads on different conditions and controller modes. The sensitivity of the quantities of interest to the input variables is discussed in groups per component (blade loads, tower bottom loads, etc.). The visualization is based on parametric swipes of the surrogate response for the entire range of each input variable. Load trends are discussed comparatively to the baseline power level.

Figure 16 shows the tower bottom load response under varying input conditions for all controller modes. The side-side load (TBMx) magnitude is highest in higher wind speeds showing an almost linear increase with increasing wind speeds in the above-rated region. Varying the power level in above-rated conditions has a minor effect on loads (<7% total variation) and the highest loads are observed for the 100% power level. The TBMx load is less damped aerodynamically and depends mainly on rotational speed, gravity, and aerodynamic torque. In the case of down-regulation using the constTSR trajectory, the lower torque leads to lower loads. In power boosting mode, the higher rotational speed leads to higher xP harmonics, which move further away from possible tower crossing frequencies reducing the loads. Using the lin70 trajectory for down-regulation has the opposite effect, increasing the TBMx load up to 7%. This increase is attributed to the decreased rotational speed in control regions 1.5 and 2, which brings the 3P harmonics of the rotor speed closer to the tower's natural frequencies leading to higher dynamic loading. The sensitivity of the DTU 10 MW rwt concerning resonances leading to increased TBMx loads has also been documented in refs. [8,19].

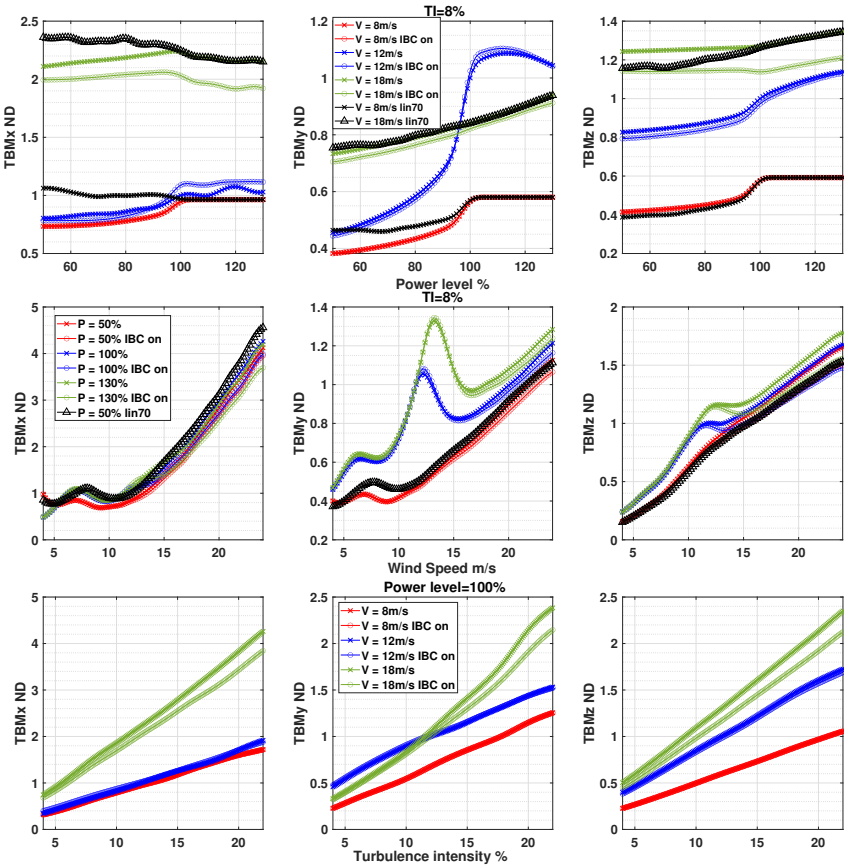

Figure 16. GPR surrogate response for the tower bottom DELs. For the power level and wind speed sensitivity plots, values are normalized with the power level of 100% at 12 m/s without IBC. For the sensitivity to TI values are normalized with the output for 12% TI at 100% power level without IBC.

Activating the IBC loop leads to TBMx load reduction to the order of 10% for all power levels. In rated and below-rated conditions, down-regulation using the constTSR trajectory leads to load reduction up to 25% for the minimum power level. The rate of reduction is higher until about 90% power level, where a 15% reduction is already reached. Conversely, the lin70 trajectory exhibits the opposite behavior, with the loads increasing with decreasing power levels due to the decrease in rotational speed. The impact of increasing TI is similar to all tower bottom loads with a linear increase in loads with increasing TI. Additionally, the effectiveness of the IBC loop is dependent on TI for all tower bottom loads. Increasing TI increases IBC load reductions proportionally to the power level.

The fore-aft tower bottom DEL, TBMy, is higher at wind speeds in the transition region as well as in the higher wind speeds, where it increases proportionally to the wind speed. In the full load region, for wind speeds above the transitions region, TBMy varies almost linearly with the power level. The maximum decrease observed is to the order of 15% for the minimum power level, while the maximum load increase is around 10% for the maximum power level. The loads in the transition region are the most sensitive to changes in power level due to the maximum thrust in this region and the transition between control regions. For maximum power boosting, TBMy load increase in this region reaches 25% and is proportional to the power level. Down-regulation with both trajectories in the transition region effectively reduces the loads by up to 50%. In the partial load region, down-regulation with constTSR reduces the loads by up to 35% while the lin70 trajectory reduces them by up to 25%. For both transition and below-rated regions and both down-regulation trajectories, more than 50% of the TBMy load reduction occurs until 90% power level. The IBC loop has a small effect on TBMy loads with a maximum load reduction of 4% for all power levels and wind speeds.

The magnitude of the torsional load at the tower bottom, TBMz, is proportional to the wind speed with a small local peak in the transition region. Power boosting increases the loads in the transition region up to a level of 20% for the maximum power level. In the full load region, the effect is smaller, with less than 5% increase for any wind speed and power level. Down-regulation in the full load region using the constTSR trajectory has practically no effect on loads, while the lin70 trajectory reduces the TBMz load up to 7%. In the partial load and transition regions, down-regulation can lead to load reductions up to 30% for the minimum power level. More than 50% of these reductions are achieved at 90% down-regulation. The application of IBC leads to TBMz load reductions to a level of 10% with the effectiveness increasing with increasing TI levels.

The tower top load response is shown in Figure 17. The roll moment load TTMx is higher for the higher wind speeds and has a significant peak in the transition region. This peak is proportional to the power level, increasing with power boosting and reducing with down-regulation. Power boosting increases the peak loads in the transition region up to 20%, proportionally to the power level. For higher wind speeds it has no impact on the TTMz loads. Down-regulation, with both trajectories, is able to reduce loads in all operating regions. In the full-load region, the load reduction is proportional to the wind speeds reaching a maximum reduction of 10–15% for the minimum power level for both trajectories. The largest load reductions by down-regulation, up to 60%, are observed in the transition region. The load reduction is proportional to the power level with a higher reduction rate until 90% power level. In the partial load region, TTMx load reduction is linearly correlated to power level. The constTSR trajectory is more effective showing a maximum load reduction of 45% for the minimum power level while for the lin70 trajectory, the reduction is up to 30%. The application of IBC does not influence TTMx loads significantly. When applied with power-boosting, IBC slightly increases the loads proportionally to the boosting level while in power levels below 80% it slightly decreases the loads. In all cases, the maximum load difference is less than 5%. All tower top loads exhibit similar trends regarding sensitivity to TI, increasing linearly with TI.

The tower top roll and pitch moment loads, TTMy and TTMz, have similar responses to the input variables and are discussed together. The load distribution over wind speeds follows the same trends with the tower bottom torsion TBMz. The load magnitude is proportional to the wind speed for the whole wind speed range with a small peak in the transition region. Power boosting increases these loads the most in the transition region up to 20% for the maximum power level. In higher wind speeds the maximum increase for any power level is lower than 8%. These increases are linearly correlated with the power level. Down-regulation in the full-load region using the constTSR trajectory does not affect loads while following the lin70 trajectory shows a reduction of up to 10% depending on the power level. In the transition and partial load regions, down-regulation can reduce the loads up to 30% and 35% considering the constTSR and lin70 trajectories, respectively. Most of the load reduction is achieved until a power level of 90% and for lower levels the load reduction rate

is significantly smaller. The IBC controller is able to reduce TTMy and TTMz loads up to 10–15% for all power levels with the effectiveness increasing proportionally to TI levels.

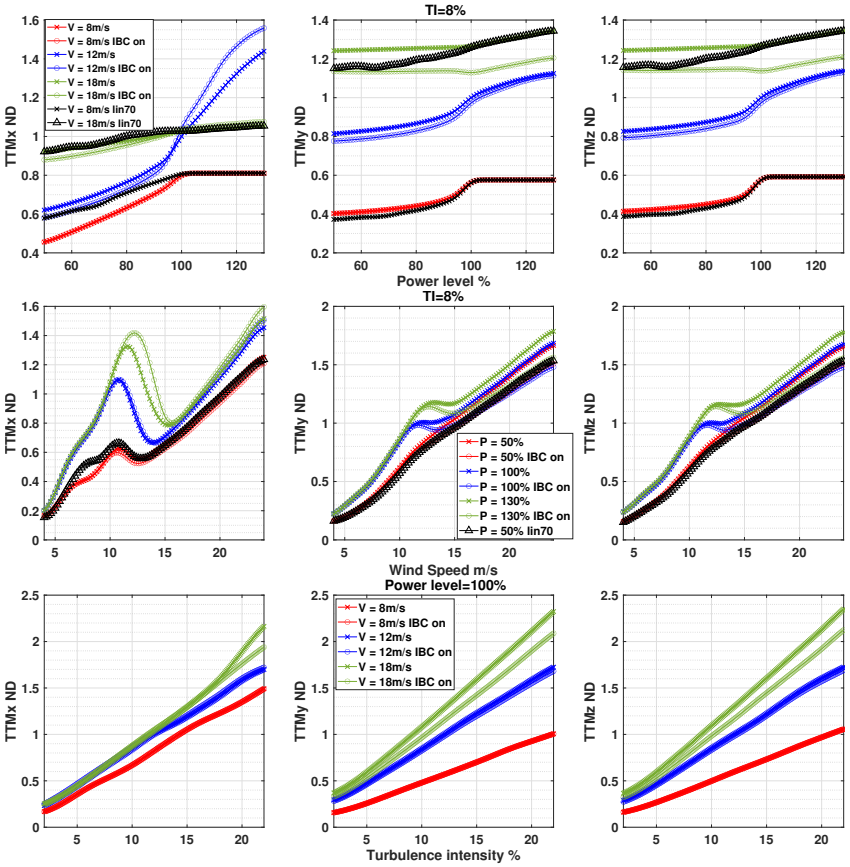

Figure 17. GPR surrogate response for the tower top/nacelle loads. For the power level and wind speed sensitivity plots, values are normalized with the power level of 100% at 12 m/s without IBC. For the sensitivity to TI, values are normalized with the output for 12% TI at 100% power level without IBC.

The sensitivity of the blade root loads to the input variables is presented in Figure 18. The edgewise bending moment load BRMx shows the least sensitivity (<10% variation in total) to all input variables. The magnitude is higher in the transition region and it is reducing in the partial and full load regions. Power boosting has a small effect increasing the BRMx loads up to 2% for the maximum power level. Similarly, down-regulation with the constTSR trajectory shows a small load reduction (<2%) for all regions and power levels. Applying the lin70 trajectory reduces BRMx loads more, in all operating regions, up to 4% due to the reduced rotational speed. The IBC controller does not affect the BRMx loads showing a reduction of up to 1% for all cases. TI does not significantly influence the BRMx DEL, with differences of less than 8% within the range considered.

The magnitude of the blade root flapwise bending moment load, BRMy, is correlated to the wind speed showing the highest values in the highest wind speeds and a significant peak in the transition region around the rated wind speed. Power boosting has the greatest impact on increasing BRMy in the transition region, with the increase reaching 20% for the maximum power level. At higher wind speeds, the maximum load increase with power boosting is 8%. In both regions, the increase is linearly correlated with the power level increase. In the full-load region, down-regulation using the constTSR trajectory does not significantly reduce the loads (<3%). In contrast, the lin70 trajectory achieves a load reduction of up to 10%, with the reduction being directly proportional to the down-regulation level. The highest load reductions with down-regulation are observed in the transition region with the lin70 trajectory showing a maximum reduction of 30% and the constTSR 25%. In the partial load region, both trajectories show similar load reductions up

to 20% for the minimum power level. In rated and below-rated regions, for both trajectories, most of the load reduction is already achieved at the 90% power level.

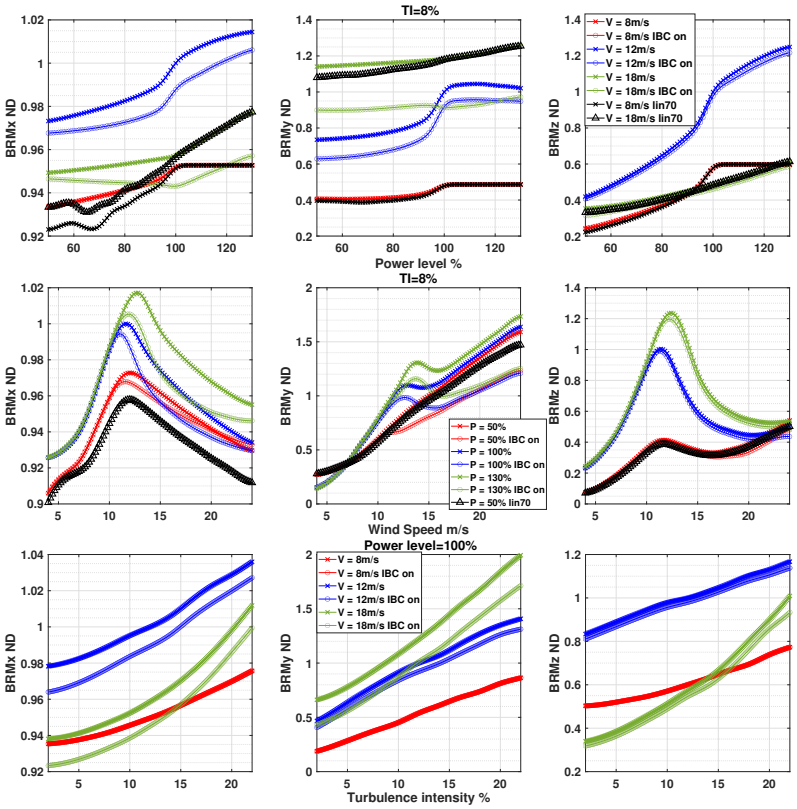

Figure 18. GPR surrogate response for the blade root loads. For the power level and wind speed sensitivity plots, values are normalized with the power level of 100% at 12 m/s without IBC. For the sensitivity to TI values are normalized with the output for 12% TI at 100% power level without IBC.

It is worth noting that for low wind speeds < 6.5 m/s and low power levels (<65%) the BRMy loads are increased compared to the baseline level, for both down-regulation trajectories. This effect was also observed for the TBMx load for wind speeds below 5 m/s. This shows the limits of down-regulation in terms of power levels for very low wind speeds in control region 1.5, as explained in Section 2.2. As expected, the IBC controller is highly effective in reducing BRMy loads since it is the controller's target load. In the higher wind speed regime IBC can reduce the loads to a level of 20–30% for all power levels while in the transition region, the load reduction is to the order of 10–15%. BRMy load magnitude presents a linear correlation to TI. In contrast to other loads discussed, the results show that the effectiveness of IBC in BRMy load reductions does not increase with TI.

The blade torsion load, BRMz, is higher in the transition region and decreases in the partial and full load. This trend changes with decreasing power levels, where for lower power levels the highest region is shifted towards the highest wind speeds. The BRMz load is sensitive to power boosting, showing an almost linear dependency on power level. For the highest power level considered, the load increase in the transition region is found to the order of 25%, and for higher wind speeds to the order of 20%. Down-regulation effectively reduces loads in all operating regions, with the two trajectories showing no significant differences. In the full-load region, the load reduction with down-regulation reaches 30% for the lowest power level, with the reduction being proportional to the down-regulation level. In the partial load and transition regions, the maximum load reduction reaches 60%, with half of it reached at the 90% power level, after which the load reduction to power level ratio reduces. The IBC controller has a negligible effect on BRMz loads. TI has a greater impact on BRMz load levels in the full load region.

The low-speed shaft loads response is presented in Figure 19. The low-speed shaft torque load LSSTq shows similar trends with the TTMx load in terms of distribution over wind speeds. The highest loads are found in the transition region and the highest wind speed region. The significant peak in the transition region increases further with power boosting and decreases substantially with down-regulation. Power boosting increases the LSSTq load only in the transition region with the magnitude of increase showing a linear correlation to the power level. The maximum increase in the peak load in the transition region is 20% with higher deltas up to 40% observed for different wind speeds in the region. This increase is the highest observed among all loads considered.

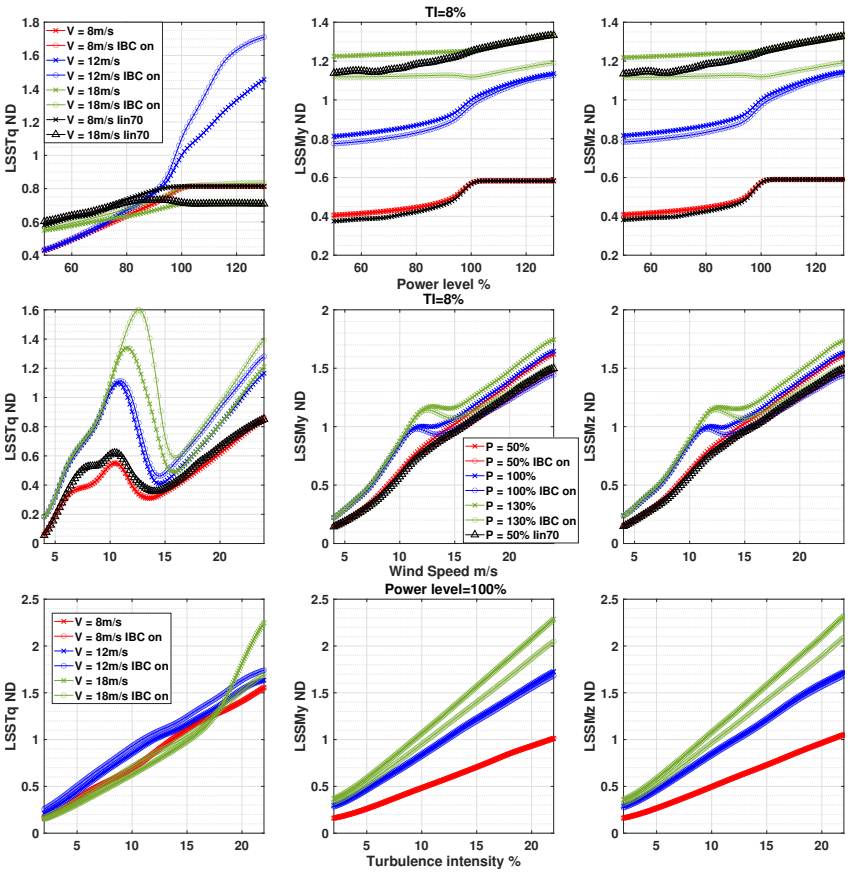

Figure 19. GPR surrogate response for the low-speed shaft loads. For the power level and wind speed sensitivity plots, values are normalized with the power level of 100% at 12 m/s without IBC. For the sensitivity to TI values are normalized with the output for 12% TI at 100% power level without IBC.

Down-regulation can reduce the LSSTq load in all operational regions. In the partial load, the reduction is linearly correlated to the power level, with a maximum reduction of 45% observed for the constTSR trajectory and 30% for the lin70 trajectory at the lowest power level. The highest load reduction is observed in the transition region with both trajectories behaving similarly, with a maximum load reduction of 55%. The rate of reduction is higher for higher power levels with 25% load reduction observed at 90% power level. In the above-rated conditions, the load reduction is linearly proportional to power level with a maximum reduction up to 25% for the constTSR trajectory and 20% for the lin70. Applying IBC has adverse effects on the LSSTq load, leading to increased magnitude. The maximum increase is found in the transition region, with a proportional relationship to the power level and a maximum value of around 20%. At higher wind speeds the increase in loads due to the IBC controller is smaller, up to 15%, and is proportional to the power level.

The low-speed shaft moment loads around the y and z axes (LSSMy and LSSMz) show very similar trends and magnitudes, and therefore, are discussed together. These loads show a similar distribution pattern to the TTMy and TTMz loads, both in terms

of wind speed and TI ranges, as well as different controller modes. The simplified drive train modeling in FAST assumes a rigid shaft, while the bearings are not modeled hence the loads are transferred directly from the shaft to the tower top node with the difference being the offset between the tower top and the shaft without any damping component in between. Power boosting increases the LSSMy and LSSMz loads primarily in the transition region. Down-regulation is effective in reducing loads, particularly in the transition and below-rated regions. The lin70 trajectory is more effective compared to the constTSR in load reduction. The IBC controller demonstrates effectiveness in load reduction at higher wind speeds, with a consistent percentage of load reduction observed across different power levels and wind speeds.

Figure 20 presents the surrogate response for mean power, energy production, and blade pitch travel. The response of power and energy over wind speeds and power levels verifies that the controller modes behave as intended in dynamic simulations. Both down-regulation and power boost modes track the power reference as intended. Furthermore, it is verified that IBC is not affecting power production. It can also be observed, using dynamic simulations instead of the steady states shown in Figure 3, how the minimum mean wind speed at which the turbine is able to produce energy, shifts. For the minimum down-regulation level, this value is approximately 5 m/s. Power is sensitive to TI with a linear correlation. In the partial load, increasing TI decreases the mean power produced with a 10% difference calculated between the lowest and highest TI values considered. In the transition region increasing TI has the opposite effect reducing the power production. The reduction is linearly correlated to TI, with a maximum reduction of 10% for the highest TI level.

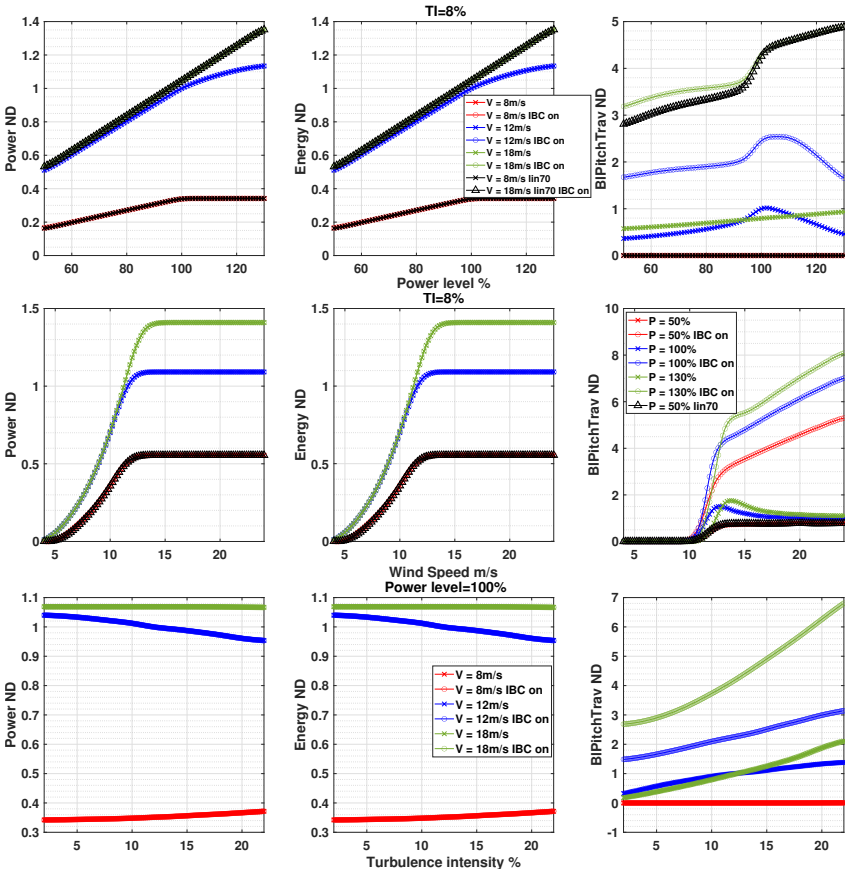

Figure 20. GPR surrogate response for electric power, energy, and blade pitch travel. For the power level and wind speed sensitivity plots, values are normalized with the power level of 100% at 12 m/s without IBC. For the sensitivity to TI values are normalized with the output for 12% TI at 100% power level without IBC.

The blade pitch travel is a simplified metric to account for pitch actuator usage. The metric aims to quantify the effect of the IBC loop and different power levels on the actuator usage over different wind conditions. Pitch travel is correlated to the power level linearly. For the maximum power level, the increase is to the order of 15–20% for all wind speeds. For the minimum power level and both down-regulation trajectories, the decrease in the full load reaches 25%. In the transition region, the difference is higher, in the order of 50%, as reducing the power levels smoothes out the turbine response in control region 2.5. The application of IBC leads to a substantial increase in blade pitch travel. The magnitude of this increase is directly proportional to wind speed for each power level. For the 100% power level, the increase varies linearly with wind speeds between 500% and 700%. The power level has a small effect on the pitch travel increase due to IBC activation. For the minimum power level, the maximum increase in pitch travel was found to the order of 660%, while for the maximum 740%. The increase in pitch travel due to the IBC application is less affected by TI with an increase of 120% within the TI range considered.

6. Discussion

The individual sensitivities of all quantities to input conditions and control modes have been discussed in the previous section. This section offers a qualitative summary of these findings, accompanied by a discussion of their implications. This discussion explores the potential trade-offs between power and loads that could be leveraged in optimization.

Table 4 provides a qualitative summary of the effects discussed. Down-regulation demonstrates greater effectiveness in load reduction within the partial load and transition regions. Conversely, its impact is less pronounced in the full load region, particularly when following the constTSR down-regulation trajectory. IBC and down-regulation serve as complementary methods for load reduction, each exhibiting efficacy in specific wind speed ranges and addressing distinct load components.

Table 4. Qualitative summary of the sensitivity of the DELs considered to the controller modes and wind conditions. PB: power boosting, DRb: down-regulation in the partial load, DRt: down-regulation in the transition region, DRa: down-regulation in the full load region, IBC: individual blade control loop activated. o: no significant change, + and ++: moderate and higher increase, – and – – moderate and higher reduction. TSR: constTSR down-regulation trajectory, lin: lin70 trajectory.

Load	DRb TSR	DRb lin	DRt TSR	DRt lin	DRa TSR	DRa lin	PB	IBC
TBMx	–	+	–	+	o	+	o	–
TBMy	– –	–	– –	–	–	–	+	o
TBMz	– –	– –	– –	– –	o	–	+	–
TTMx	– –	–	– –	–	–	o	++	+
TTMy	– –	– –	– –	– –	o	–	+	–
TTMz	– –	– –	– –	– –	o	–	+	–
BRMx	o	–	o	–	o	o	o	o
BRMy	– –	– –	– –	– –	o	o	+	– –
BRMz	– –	– –	– –	– –	–	–	++	o
BROop	– –	– –	– –	– –	o	–	+	– –
BRIp	o	–	o	–	o	o	o	o
LSSTq	– –	o	– –	– –	–	–	++	++
LSSMy	– –	– –	– –	– –	o	–	+	–
LSSMz	– –	– –	– –	– –	o	–	+	–

The TBMx, BRMx, and BRIp loads exhibit the least sensitivity across all control modes. Moreover, TBMy, TTMx, BRMz, and LSSTq loads are found to increase the most when power boosting is applied. The activation of IBC results in substantial reduction in blade BRMy and BROOp loads, with moderate reductions in TBMx, TBMZ, TTMy, TTMz, LSSMy, and LSSMz. For the rest of the loads, it is observed that activating IBC has either no effect (TBMy and BRMz) or increases the load in the same region where power boosting has the greatest impact (TTMx, LSSTq). The findings suggest that selectively implementing IBC

at higher wind speeds than the transition region could be advantageous, as it lowers the impact on adversely affected loads. For loads positively influenced by IBC, its effectiveness is consistent across the entire applicable wind speed range.

A significant portion of the expected load reduction achieved through down-regulation is associated with a small decrease in power level. This can be attributed to the steep C_p peak in the $\lambda - \theta$ space (see Figure 2). The analysis conducted previously revealed that, for the DTU 10 MW rwt aerodynamic design, over 50% of the maximum load reduction can be accomplished with a down-regulation level of 90% for the majority of loads. Conversely, at lower down-regulation levels, the rate of load reduction per power level diminishes significantly. This indicates that the trade-off between power and loads is more favorable in this particular region. Further reductions in power yield diminishing effects, as a small load reduction is accompanied by greater losses in power production. This effect was primarily observed when applying down-regulation in wind speeds within the transition and below-rated regions for the TBMx, TBMy, TBMz, TTMy, TTMz, BRMy, BRMz, LSSMy, and LSSMz loads.

The transition region, between partial and full load, is highly sensitive in terms of loads, regardless of the controller design and the switching logic. Implementing down-regulation within this region has a smoothing effect on the transition, resulting in significant load reduction in most cases. This observation is further supported by measurement data, as shown in [13]. Leveraging this insight in a potential optimization suggests that a small decrease in power level within the transition region can yield an overall significant reduction in loads, with a relatively smaller energy production loss.

An additional factor that can be utilized in optimization is grouping loads that exhibit similar responses to the control modes. Defining a load ensemble for the load evaluation function is essential for optimization. Loads that demonstrate similar behavior can be grouped and one load from the group can be selected as representative. This approach can reduce the number of optimization variables and enhance the efficiency of the process. The analysis conducted in the previous section revealed that the TBMz, TTMy, TTMz, LSSMy, and LSSMz loads exhibit very similar responses and can be effectively used for this purpose. LSSTq and TTMx also display similar responses, particularly in the transition and partial load regions, although the correlation is weaker compared to the previous group.

Comparing the two trajectories considered for down-regulation setpoint derivation, it was observed that the choice of trajectory has an impact on the loads. By maintaining constant rotational speed and performing down-regulation employing only the blade pitch, the constTSR trajectory exhibited higher load reduction per power level for the TBMX, TBMy, TTMx, and LSSTq loads. On the other hand, combining both torque and rotational speed in the lin70 trajectory resulted in higher load reduction for TBMz, BRMy, TTMy, TTMz, LSSMY, and LSSMz loads. This effect was particularly prominent in the full load region, suggesting that further rotational speed reduction may be beneficial for load reduction in this wind speed region.

Especially for trajectories involving rotational speed reduction, it was found that there is a limit to the minimum assignable power level due to the impact of reduced rotational speed on region 1.5, cut-in wind speed, and loads. In this region, the turbine operates off-design and can exhibit unpredictable behavior, particularly at lower power levels (<70%) where accurate power tracking becomes challenging and load dependence on power level diminishes. Moreover, reducing rotational speed alters the effective cut-in wind speed, and this effect becomes more prominent for lower power levels in trajectories relying on rotational speed reduction. This information holds greater significance when considering down-regulation for optimal power tracking, such as in scenarios where significant curtailment is required by the grid operator. However, in cases where load reduction is the objective or in wind farm control scenarios targeting thrust reduction, such low levels of down-regulation may not yield meaningful outcomes. Furthermore, considering the stiff-stiff tower design combined with low structural damping, it is crucial to prevent the excitation of tower frequencies. Resonances, particularly in the low-damped tower side-side loads, can occur when turbulence is combined with a lower TSR.

The trends identified here are focused on the specific aerodynamic and structural design of the DTU 10 MW reference wind turbine as well as the proposed controller design. Nevertheless, they are expected to carry over to other machines of similar size and structural design, although possibly with different magnitudes. For machines with significantly larger (and possibly more flexible rotors) or different aerodynamic or structural designs of the components (e.g., a not stiff-stiff tower design as in the case of the DTU 10 MW) the impact of the control modes on the structural loads has to be evaluated on the specific design. Moreover, the turbine is considered in an onshore configuration. The derived trends are expected to be valid also in an offshore fixed-bottom setup. A limited simulation performed by the authors showed very similar trends to most loads considered with the addition of hydrodynamics affecting mainly the monopile substructure loads.

7. Conclusions

The goal of this study was to develop and evaluate surrogate models for a multi-MW VSPR modern wind turbine with down-regulation, power boosting, and IBC control modes. The controller tuning was discussed for all modes. Two down-regulation trajectories, based on pitching only and a combination of pitching and rotational speed reduction were explored for power level reduction up to 50%. Power boosting was performed by following the maximum C_p curve for power levels up to 130%. The IBC loop includes an independent SISO controller for each blade feedbacking the blade root flapwise bending moment.

The response of the entire turbine system including power, loads, and pitch actuation metrics was captured by aeroelastic simulations employing a dense full factorial sampling approach for wind speed, TI, and controller mode. Based on this simulation database two methods were compared for creating a data-driven surrogate model. Although computationally cheaper the spline-based interpolation showed to perform very similar to the more expensive GPR model considered, possibly due to the dense sampling. As the spline-based approach is faster to implement and generate predictions with, it would be preferred for cases where multiple evaluations are required while the GPR model could be beneficial in cases where probabilistic assessment is considered since it can directly provide uncertainty estimates. The comparison to a validation set showed low uncertainty across all quantities considered with a mean absolute error lower than 4% with the very low wind speed and transition regions showing the highest uncertainty in most cases.

Using the surrogate model, a thorough aeroelastic analysis of the entire system was performed discussing the trends across wind conditions and controller modes. The loads and wind speed regions influenced the most by each control mode were identified. The analysis showed that the difference between the two down-regulation trajectories is relatively small affecting the distribution of load reductions across the different components. Down regulation showed to be more effective in load reduction in the transition region for most loads while the majority of load reductions were observed until 90% power levels. These insights can be leveraged for optimization purposes focusing on fatigue and possibly revenue management. Moreover, the combination of down-regulation and IBC showed to be synergistic in terms of potential load reductions as they are more effective in different wind speed regions and loads, showing that they can be combined to effectively reduce the majority of loads in the system. The loads affected the most by power boosting were identified, with the trends showing that load increase is proportional to the power level.

Overall, the models and results presented in this work can enable tasks such as condition monitoring and operational optimization at a system level by offering quick and accurate surrogate models that capture multiple controller modes relevant to wind turbine operation.

Author Contributions: Conceptualization, Methodology, Software, Writing—original draft V.P.; Writing—review P.W.C. All authors have read and agreed to the published version of the manuscript.

Funding: This study was funded by Stiftung Energieforschung Baden-Württemberg within the research project Wind Farm Optimized Operation (WOOP) (grant number: A341 21), which is gratefully acknowledged for the financial support.

Data Availability Statement: The training and validation sets, along with the trained GPR models and relevant scripts for generating the predictions of the surrogate model, are publicly available at https://doi.org/10.5281/zenodo.10092271 (accessed on 28 February 2024).

Conflicts of Interest: The authors declare no conflict of interest.

Abbreviations

The following abbreviations are used in this manuscript:

BRMx	Edgewise blade root moment
BRMy	Flapwise blade root moment
BRMz	Blade root torsion
BROop	Out of plane blade root moment
BRIp	In plane blade root moment
TBMx	Fore-aft tower bottom moment
TBMy	Side-side tower bottom moment
TBMz	Tower bottom torsion
TTMx	Tower top roll moment
TTMy	Tower top pitch moment
TTMz	Tower top yaw moment
LSSMy	Low-speed shaft moment around y-axis
LSSMz	Low-speed shaft moment around z-axis
LSSTq	Low-speed shaft torque
DEL	Damage equivalent load
ND	Non-dimensional
TI	Turbulence intensity
PitchTr	Blade pitch travel
IPC	Individual Pitch Control
IBC	Individual Blade Control
CPC	Collective pitch controller
PI	Proportional Integral
K_p	Proportional gain
T_i	Inverse of integral gain
DOE	Design of Experiment
TSR	Tip speed ratio
MAE	Mean absolute error
ME	Mean error
MedAE	Median absolute error
R^2	Coefficient of determination
P	Electrical power
P_{nom}	Nominal electrical power
P_{rated}	Rated electrical power
C_p	Power coefficient
C_t	Thrust coefficient
Act	Blade pitch actuator
θ	Pitch angle
θ_{CPC}	Pitch angle commanded by the collective pitch controller
θ_{max}	Maximum pitch angle
ω_{rot}	Rotor rotational speed
$\omega_{g,rated}$	Rated generator rotational speed
$\omega_{g,filt}$	Filtered generator rotational speed
$\omega_{g,min}$	Minimum generator rotational speed
$\omega_{g,max}$	Maximum generator rotational speed
$\omega_{g,max15}$	Maximum generator rotational speed in control region 1.5
ω_g	Generator rotational speed
M_g	Generator torque
$M_{g,min}$	Minimum generator torque
$M_{g,max}$	Maximum generator torque
$M_{g,com}$	Commanded generator torque

$M_{g,rat}$	Rated generator torque
k	Constant for the torque controller
HP	High-pass filter
BS	Band-stop filter
LP	Low-pass filter
τ	Time constant of the first-order low-pass filter
ξ_f	damping ratio of second-order low-pass filter
$\omega_{N,f}$	natural frequency of second-order low-pass filter
a_{15}	Offset of linear ramp for control region 1.5
b_{15}	Slope of linear ramp for control region 1.5
e	Error from setpoint

Appendix A. Kernel and Basis Radial Function for the GPR Model

Table A1. Kernel function and basis function for GPR for the different quantities of interest found by hyperparameter optimization.

Quantity	Kernel Function	Basis Function
BRMx	Matern32	Linear
BRMy	Matern32	Constant
BRMz	Matern52	Linear
BROop	Matern32	Quadratic
BRIp	Matern32	Linear
TBMx	Matern32	None
TBMy	Matern32	Linear
TBMz	Matern32	Linear
TTMx	Matern32	Linear
TTMy	Matern52	None
TTMz	Matern32	Linear
LSSMy	Matern32	Linear
LSSMz	Matern32	Linear
LSSTq	RationalQuadratic	None
Power	Matern32	Constant
Energy	Exponential	Quadratic
PitchTr	Matern32	None

References

1. Eguinoa, I.; Göçmen, T.; Garcia-Rosa, P.B.; Das, K.; Petrović, V.; Kölle, K.; Manjock, A.; Koivisto, M.J.; Smailes, M. Wind farm flow control oriented to electricity markets and grid integration: Initial perspective analysis. *Adv. Control Appl.* **2021**, *3*, 1–28. [CrossRef]
2. Meyers, J.; Bottasso, C.; Dykes, K.; Fleming, P.; Gebraad, P.; Giebel, G.; Göçmen, T.; van Wingerden, J.W. Wind farm flow control: Prospects and challenges. *Wind Energy Sci.* **2022**, *7*, 2271–2306. [CrossRef]
3. Ziegler, L.; Gonzalez, E.; Rubert, T.; Smolka, U.; Melero, J.J. Lifetime extension of onshore wind turbines: A review covering Germany, Spain, Denmark, and the UK. *Renew. Sustain. Energy Rev.* **2018**, *82*, 1261–1271. [CrossRef]
4. Pettas, V.; Cheng, P.W. Down-regulation and individual blade control as lifetime extension enablers. *J. Phys. Conf. Ser.* **2018**, *1102*, 012026. [CrossRef]
5. Requate, N.; Meyer, T.; Hofmann, R. From wind conditions to operational strategy: Optimal planning of wind turbine damage progression over its lifetime. *Wind. Energy Sci. Discuss.* **2023**, *8*, 1727–1753. [CrossRef]
6. Kölle, K.; Göçmen, T.; Eguinoa, I.; Alcayaga Román, L.A.; Aparicio-Sanchez, M.; Feng, J.; Meyers, J.; Pettas, V.; Sood, I. FarmConners market showcase results: Wind farm flow control considering electricity prices. *Wind Energy Sci.* **2022**, *7*, 2181–2200. [CrossRef]
7. Simley, E.; Millstein, D.; Jeong, S.; Fleming, P.A. The value of wake steering wind farm control in U.S. energy markets. *Wind. Energy Sci.* **2023**, 1–26.
8. Bak, C.; Zahle, F.; Bitsche, R.; Yde, A.; Henriksen, L.C.; Nata, A.; Hansen, M.H. *Description of the DTU 10 MW Reference Wind Turbine, DTU Wind Energy Report-I-0092*; Technical Report July; DTU: Roskilde, Denmark, 2013.
9. Aho, J.; Fleming, P.; Pao, L.Y. Active power control of wind turbines for ancillary services: A comparison of pitch and torque control methodologies. In Proceedings of the 2016 American Control Conference (ACC), Boston, MA, USA, 6–8 July 2016; pp. 1407–1412.
10. Astrain Juangarcia, D.; Eguinoa, I.; Knudsen, T. Derating a single wind farm turbine for reducing its wake and fatigue. *J. Phys. Conf. Ser.* **2018**, *1037*, 032039. [CrossRef]

11. Lio, W.H.; Mirzaei, M.; Larsen, G.C. On wind turbine down-regulation control strategies and rotor speed set-point. *J. Phys. Conf. Ser.* **2018**, *1037*, 032040. [CrossRef]
12. Mirzaei, M.; Tibaldi, C.; Hansen, M.H. PI controller design of a wind turbine: Evaluation of the pole-placement method and tuning using constrained optimization. *J. Phys. Conf. Ser.* **2016**, *753*, 052026. [CrossRef]
13. Kretschmer, M.; Pettas, V.; Cheng, P.W. Effects of Wind Farm Down-Regulation in the Offshore Wind Farm Alpha Ventus. In Proceedings of the ASME 2019 2nd International Offshore Wind Technical Conference, St. Julian's, Malta, 3–6 November 2019.
14. Galinos, C.; Larsen, T.J.; Mirzaei, M. Impact on wind turbine loads from different down regulation control strategies. *J. Phys. Conf. Ser.* **2018**, *1104*, 012019. [CrossRef]
15. Solum, A.; Leijon, M. Investigating the overload capacity of a direct-driven synchronous permanent magnet wind turbine generator designed using high-voltage cable technology. *Int. J. Energy Res.* **2007**, *31*, 1076–1086. [CrossRef]
16. Siemens Gamesa AS. Siemens Gamesa Power Boost Technology WebPage, Brochure. 2020. Available online https://www.siemensgamesa.com/products-and-services/offshore/wind-turbine-sg-14-222-dd (accessed on 15 December 2023).
17. Vestas. Vestas Power Uprate. Available online: https://nozebra.ipapercms.dk/Vestas/Communication/Productbrochure/ProductImprovements/PowerUprate/ (accessed on 15 December 2023).
18. Siemens. Siemens Energy Thrust. Available online: https://www.siemensgamesa.com/products-and-services/service-wind/energy-thrust (accessed on 15 December 2023).
19. Pettas, V.; Barlas, T.; Gertz, D.; Madsen, H.A. Power performance optimization and loads alleviation with active flaps using individual flap control. *J. Phys. Conf. Ser.* **2016**, *749*, 012010. [CrossRef]
20. Bossanyi, E.A. Individual Blade Pitch Control for Load Reduction. *Wind Energy* **2003**, *6*, 119–128. [CrossRef]
21. Bossanyi, E.A. Further load reductions with individual pitch control. *Wind Energy* **2005**, *8*, 481–485. [CrossRef]
22. Lio, W.H.; Jones, B.L.; Lu, Q.; Rossiter, J.A. Fundamental performance similarities between individual pitch control strategies for wind turbines. *Int. J. Control* **2017**, *90*, 37–52. [CrossRef]
23. Bossanyi, E.A.; Fleming, P.A.; Wright, A.D. Validation of Individual Pitch Control by Field Tests on Two- and Three-Bladed Wind Turbines. *IEEE Trans. Control Syst. Technol.* **2013**, *21*, 1067–1078. [CrossRef]
24. Ossmann, D.; Seiler, P.; Milliren, C.; Danker, A. Field testing of multi-variable individual pitch control on a utility-scale wind turbine. *Renew. Energy* **2021**, *170*, 1245–1256. [CrossRef]
25. Pettas, V.; Salari, M.; Schlipf, D.; Cheng, P.W. Investigation on the potential of individual blade control for lifetime extension. *J. Phys. Conf. Ser.* **2018**, *1037*, 032006. [CrossRef]
26. Schlipf, D. Lidar-Assisted Control Concepts for Wind Turbines. Ph.D. Thesis, Stuttgart University, Stuttgart, Germany, 2016.
27. Barlas, T.; Pettas, V.; Gertz, D.; Madsen, H.A. Extreme load alleviation using industrial implementation of active trailing edge flaps in a full design load basis. *J. Phys. Conf. Ser.* **2016**, *753*, 042001. [CrossRef]
28. Forrester, A.I.J.; Sóbester, A.; Keane, A.J. *Engineering Design via Surrogate Modelling*; Wiley: Hoboken, NJ, USA, 2008.
29. Dimitrov, N.; Kelly, M.C.; Vignaroli, A.; Berg, J. From wind to loads: Wind turbine site-specific load estimation with surrogate models trained on high-fidelity load databases. *Wind Energy Sci.* **2018**, *3*, 767–790. [CrossRef]
30. Slot, R.M.; Sørensen, J.D.; Sudret, B.; Svenningsen, L.; Thøgersen, M.L. Surrogate model uncertainty in wind turbine reliability assessment. *Renew. Energy* **2020**, *151*, 1150–1162. [CrossRef]
31. Rinker, J.M. Calculating the sensitivity of wind turbine loads to wind inputs using response surfaces. *J. Phys. Conf. Ser.* **2016**, *753*, 032057. [CrossRef]
32. Murcia, J.P.; Réthoré, P.E.; Dimitrov, N.; Natarajan, A.; Sørensen, J.D.; Graf, P.; Kim, T. Uncertainty propagation through an aeroelastic wind turbine model using polynomial surrogates. *Renew. Energy* **2018**, *119*, 910–922. [CrossRef]
33. Bortolotti, P.; Canet, H.; Bottasso, C.L.; Loganathan, J. Performance of non-intrusive uncertainty quantification in the aeroservoelastic simulation of wind turbines. *Wind Energy Sci.* **2019**, *4*, 397–406. [CrossRef]
34. Barlas, T.; Ramos-García, N.; Pirrung, G.R.; González Horcas, S. Surrogate-based aeroelastic design optimization of tip extensions on a modern 10 MW wind turbine. *Wind Energy Sci.* **2021**, *6*, 491–504. [CrossRef]
35. Gasparis, G.; Lio, W.H.; Meng, F. Surrogate Models for Wind Turbine Electrical Power and Fatigue Loads in Wind Farm. *Energies* **2020**, *13*, 6360. [CrossRef]
36. Dimitrov, N. Surrogate models for parameterized representation of wake-induced loads in wind farms. *Wind Energy* **2019**, *22*, 1371–1389. [CrossRef]
37. Debusscher, C.M.J.; Göçmen, T.; Andersen, S.J. Probabilistic surrogates for flow control using combined control strategies. *J. Phys. Conf. Ser.* **2022**, *2265*, 032110. [CrossRef]
38. Jonkman, J.M.; Buhl, M.L.J. *FAST User's Guide—Updated August 2005*; Technical Report 6; National Renewable Energy Laboratory (NREL): Golden, CO, USA, 2005.
39. van der Hoek, D.C.; Kanev, S. *Reducing Wind Turbine Loads with Down-Regulation*; Technical Report ECN-E–17-032, ECN-E–17-032; Energy Research Centre of the Netherlands: Petten, The Netherlands, 2017.
40. Leithead, W.E.; Neilson, V.; Dominguez, S.; Dutka, A. A novel approach to structural load control using intelligent actuators. In Proceedings of the 17th Mediterranean Conference on Control & Automation, Thessaloniki, Greece, 24–26 June 2009; pp. 1257–1262.
41. Han, Y.; Leithead, W.E. Comparison of Individual Blade Control and Individual Pitch Control for Wind Turbine Load Reduction. In Proceedings of the European Wind Energy Association (EWEA) Conference 2015, Paris, France, 17–20 November 2015.

42. International Electrotechnical Commision (IEC). *Wind Turbines Part 1: Design Requirements 61400-1*, 3rd ed.; Technical Report; International Electrotechnical Commision (IEC): Geneva, Switzerland, 2005.
43. Müller, K. Probabilistic Fatigue Load Assessment for Floating Wind Turbines. Ph.D. Thesis, University of Stuttgart, Stuttgart, Germany, 2019.
44. Robertson, A.N.; Shaler, K.; Sethuraman, L.; Jonkman, J. Sensitivity analysis of the effect of wind characteristics and turbine properties on wind turbine loads. *Wind Energy Sci.* **2019**, *4*, 479–513. [CrossRef]
45. NREL FAST v8. Available online: https://www.nrel.gov/wind/nwtc/fastv8.html (accessed on 15 December 2023).
46. Borg, M.; Mirzaei, M.; Bredmose, H. *LIFES50+ Deliverable D1.2 Wind Turbine Models for the Design*; Technical Report; 2015. Available online: https://lifes50plus.eu/results/ (accessed on 15 December 2023).
47. NREL. Turbsim Legacy Web Page. Available online: https://www.nrel.gov/wind/nwtc/turbsim.html (accessed on 15 December 2023).
48. Miner, M. Cumulative Damage in Fatigue. *J. Appl. Mech.* **1945**, *3*, 159–164. [CrossRef]
49. Rychlik, I. A new definition of the rainflow cycle counting method. *Int. J. Fatigue* **1987**, *9*, 119–121. [CrossRef]
50. McKay, M.D.; Beckman, R.J.; Conover, W.J. A Comparison of Three Methods for Selecting Values of Input Variables in the Analysis of Output from a Computer Code. *Technometrics* **1979**, *21*, 239.
51. Rasmussen, C.E.; Williams, C.K.I. *Gaussian Processes for Machine Learning*; The MIT Press: Cambridge, MA, USA, 2005.

Disclaimer/Publisher's Note: The statements, opinions and data contained in all publications are solely those of the individual author(s) and contributor(s) and not of MDPI and/or the editor(s). MDPI and/or the editor(s) disclaim responsibility for any injury to people or property resulting from any ideas, methods, instructions or products referred to in the content.